Title

Function and firing of the *Streptomyces coelicolor* contractile injection system requires the membrane protein CisA

Authors

Bastien Casu[1], Joseph W. Sallmen[2], Peter E. Haas[1], Govind Chandra[1], Pavel Afanasyev[1], Jingwei Xu[1], Susan Schlimpert[2, *], Martin Pilhofer[1, *]

Short title

A membrane protein enables *Streptomyces* contractile injection system firing

Affiliations

[1]Department of Biology, Institute of Molecular Biology & Biophysics, Eidgenössische Technische Hochschule Zürich, Otto-Stern-Weg 5, 8093 Zürich, Switzerland

[2]John Innes Center, Department of Molecular Microbiology, Norwich Research Park, Norwich, NR4 7UH, United Kingdom

Contact Info

* Correspondence: Susan.Schlimpert@jic.ac.uk (S.S.) and pilhofer@biol.ethz.ch (M.P.)

Abstract

Bacterial contractile injection systems (CIS) are phage tail-like macromolecular complexes that mediate cell-cell interactions by injecting effector proteins into target cells. CIS from *Streptomyces coelicolor* (CIS^{Sc}) are localized in the cytoplasm. Under stress, they induce cell death and impact the bacteria's life cycle. It remains unknown whether CIS^{Sc} require accessory proteins to directly interact with the cytoplasmic membrane and function.

Here, we characterize the putative membrane adaptor CisA, a conserved factor in *CIS* gene clusters across *Streptomyces* species. We show by cryo-electron tomography imaging and *in vivo* assays that CIS^{Sc} contraction and function depend on CisA. Using single-particle cryo-electron microscopy, we provide an atomic model of the extended CIS^{Sc} apparatus; however, CisA is not part of the complex. Instead, our findings show that CisA is a membrane protein with a cytoplasmic N-terminus predicted to interact with CIS^{Sc} components, thereby providing a possible mechanism for mediating CIS^{Sc} recruitment to the membrane and subsequent firing.

Our work shows that CIS function in multicellular bacteria is distinct from Type 6 Secretion Systems and extracellular CIS, and possibly evolved due to the role CIS^{Sc} play in regulated cell death.

Keywords: bacterial development/cellular microbiology/contractile phage tail/ghost cells/multicellularity

Introduction

Bacteria employ different types of contractile injection systems (CIS) to mediate cell-cell interactions or to mediate cell death (1). CIS are evolutionarily and structurally related to contractile tails of bacteriophages and are comprised of core modules including a baseplate, a contractile sheath, and an inner tube (2,3). CIS firing is triggered by a conformational change within the baseplate (4,5) and results in the contraction of the sheath, which in turn propels the inner tube along with the spike tip. Tube expulsion facilitates the release of associated effector proteins into target cells or the extracellular space (6,7).

Bioinformatic analyses have shown that CISs are conserved across diverse microbial phyla, including Gram-negative and Gram-positive bacteria, as well as archaea (8,9). Based on their distinct modes of action, CIS can be categorized into two main groups: intracellular type VI secretion systems (T6SS) and extracellular CIS (eCIS). T6SS are abundant among Gram-negative bacteria and in some archaea, and they are anchored to the cytoplasmic membrane during assembly and firing (10–12). A crucial component of the T6SS is the baseplate, which acts as a nucleus for T6SS assembly and mediates the binding of the T6SS particles to the cytoplasmic membrane until contraction. Upon contraction, the spike and inner tube are propelled out of the cell into an adjacent cell or the medium. eCIS, on the other hand, are assembled as free-floating particles in the cytoplasm and are subsequently released into the extracellular space upon lysis of the producer cell (13–16). Following the release, eCIS attach to the surface of target cells via their tail fibers, followed by contraction and puncturing of the target cell envelope.

Besides T6SS and eCIS, there is accumulating evidence of additional CIS assemblies with distinct modes of action in bacteria. For example, in multicellular cyanobacteria, CIS are anchored to the intracellular thylakoid membrane stacks via an extension of the baseplate components and have been proposed to function in cell lysis and the formation of “ghost cells” in response to stress conditions (17). Furthermore, several recent studies reported the production of free-floating cytoplasmic CIS particles in the multicellular Gram-positive *Streptomyces* bacteria, which have been shown to modulate cellular development through presumably slightly different mechanisms (18–22).

68 *Streptomyces* are best known for producing a plethora of medically and industrially important
69 secondary metabolites, including molecules with antimicrobial, antifungal, anticancer or
70 immunosuppressive properties. The production of these molecules is tightly coordinated with
71 the *Streptomyces* developmental life cycle that encompasses two filamentous cell types:
72 vegetative hyphae that grow by tip extension and branching to scavenge for nutrients, and
73 reproductive (aerial) hyphae that eventually differentiate into chains of spores, which can then
74 be dispersed to restart the life cycle (23,24). Using *Streptomyces coelicolor* as a model
75 organism, we and others previously demonstrated that *S. coelicolor* CIS (CIS^{Sc}) mediate a form
76 of regulated cell death, which influences the onset of sporulation and secondary metabolite
77 production in response to exogenous stress and unknown cellular signals (Figure 1a) (18,19).

78 It remains unclear whether CIS^{Sc} contraction occurs while the CIS^{Sc} particles are free-floating
79 in the cytoplasm or whether this depends on an interaction with the membrane. Moreover, CIS
80 encoded in *Streptomyces* genomes lack clear homologs for tail fiber components or a T6SS
81 trans-envelope complex, raising the question of how CIS^{Sc} particles could potentially interact
82 with the cytoplasmic membrane. We and others recently noted an uncharacterized protein
83 (18,19), SCO4242, which is conserved in the majority of *Streptomyces* species and other
84 Actinomycete species that carry a type IId eCIS locus (8,9) (Supplementary Fig. 1 and
85 Supplementary Data 1 and 2). Interestingly, SCO4242 is encoded just downstream of the
86 baseplate components in the CIS^{Sc} gene cluster, a location that usually encodes tail fibers from
87 conventional eCIS (13,16,25). We will, therefore, refer to the gene product of SCO4242 as
88 CisA for "CIS^{Sc}-associated protein A." Here, we set out to assess the importance of CisA for
89 CIS^{Sc} function and its possible role as a membrane anchor.

90 # Results

91 ## CisA is required for CIS^{Sc} contraction *in situ*

92 To explore the role of CisA (SCO4242) in CIS^{Sc} contraction and function, we first generated
93 an *S. coelicolor* Δ*cisA* null mutant. Negative stain electron microscopy (EM) imaging of CIS^{Sc}
94 particles that were purified from Δ*cisA* mutant cells showed assemblies in the contracted
95 conformation, similar to the CIS particles purified from the wild type (WT) (Fig. 1b/c). We
96 then imaged vegetative hyphae of the WT, the Δ*cisA* mutant and the complemented mutant
97 (Δ*cisA/cisA*$^{+}$) by cryo-electron tomography (cryoET) (270 tomograms in total, n=3
98 experiments). The observed CIS^{Sc} particles in intact hyphae of these three imaged strains did
99 not reveal discernable differences, indicating that CisA is not required for CIS^{Sc} assembly. We
100 previously showed that CIS^{Sc} contraction is linked to cell death in *S. coelicolor* wildtype
101 hyphae and we observed a clear shift in the number of extended to fully contracted CIS^{Sc}
102 particles in damaged and dead hyphae (ghost cells) (18). Interestingly, and in contrast to the
103 WT and complemented *cisA* mutant strain (Fig. 1d and f), *cisA*-deficient hyphae only contained
104 CIS^{Sc} particles in the extended conformation irrespective of the cellular integrity of the hyphae
105 (Fig. 1e, Supplementary Fig. 2a-d). While hyphal cell death can be induced by a range of
106 different external or internal factors, our results suggest that CisA is required for the contraction
107 of CIS^{Sc} *in situ*.

108 ## CryoEM structure of the extended CIS^{Sc} assembly

109 Contractile injection systems are generally classified into intracellular type VI secretions
110 systems (T6SS) and the superfamily of extracellular CIS (eCIS), which is subdivided into six
111 families with distinct genetic compositions (8). Many *Streptomyces* genomes contain a class
112 IId eCIS locus, a subtype that is structurally less well understood compared to other eCIS
113 subtypes, which includes 'antifeeding prophages' (AFPs) from *Serratia*, 'metamorphosis-
114 associated contractile structures' (MACs) from *Pseudoalteromonas luteoviolacea*, AlgoCIS
115 from *A. machipongonensis* or '*Photorhabdus* virulence cassettes' (PVCs) from *P. asymbiotica*
116 (1).

117 The CIS^{Sc} gene cluster consists of 19 predicted open reading frames (accessions *SCO4242-*
118 *4260*) (Fig. 2a), including genes with sequence similarities to potential CIS structural

119 components (*cis1-cis16*), as well as additional genes with unknown functions (including *cisA*)
120 (18,19). To determine whether CisA is an integral component of CIS^{Sc}, we set out to elucidate
121 the high-resolution structure of purified CIS^{Sc} particles from a non-contractile CIS^{Sc} mutant
122 (18). The purified assemblies were subjected to single particle cryo-electron microscopy
123 (cryoEM) for structure determination (Supplementary Fig. 3), yielding the first high-resolution
124 model of the CIS^{Sc} in its extended conformation, which also presents the first example of a CIS
125 IId subtype (8).

126 Our model shows that extended CIS^{Sc} particles share the conserved eCIS architecture,
127 including three modules: cap, sheath-tube and baseplate (Fig. 2b). We processed the dataset
128 using an established workflow that was previously employed to produce the atomic model for
129 other CIS (Supplementary Fig. 3) (13,17). The resulting maps of the baseplate and the cap
130 reached resolutions of 3.5 and 3.4 Å, respectively. The quality of the final maps from the two
131 modules enabled *de novo* structural modelling (Supplementary Fig. 4, Supplementary Table
132 1).

133 The final model of CIS^{Sc} comprised 783 polypeptide chains that assemble into a bullet-shaped
134 particle measuring 268 nm in length (Fig. 2b/c). All analyzed particles were identical in length,
135 consistent with our *in situ* data of extended CIS^{Sc} particles in vegetative hyphae of WT *S.*
136 *coelicolor* (Fig. 1d-f). The length of eCIS particles is often controlled by tape measure proteins
137 (26), we note, however, that the corresponding gene is absent from the CIS^{Sc} gene cluster. The
138 distal end of the CIS^{Sc} is capped by a tail terminator complex (Fig. 2c/e). This cap comprises
139 one protein, Cis16, forming a C6-symmetrical complex that terminates the inner tube and
140 sheath, respectively. This minimal architecture resembles the cap complexes of PVC or Pyocin
141 R2 CISs, but it is different from the more complex AlgoCIS from *A. machipongonensis* and
142 AFP from *S. entomophila* (Supplementary Fig. 5) (13,16,25,27). The structures of the CIS^{Sc}
143 sheath-tube module have been discussed previously (18). Here we found that the module
144 consists of 61 sheath layers (Cis2-L_1–L_{61}) and 60 tube layers (Cis1-L_1-L_{60}) (Fig. 2b/d).

145 The baseplate module comprises a heteromeric assembly of the proteins Cis1b/7/8/9/11/12
146 (Fig. 2b/c). The symmetry transition from the inner tube (Cis1a, C6) to the VgrG-like spike
147 (Cis8, C3) is adapted by two layers of the tube initiators Cis1b and Cis7. The first layer of the
148 sheath (Cis2) is bound to the conserved gp25-like protein Cis9, which connects to the baseplate
149 'wedges' composed of Cis11 and Cis12 (Fig. 2b/c). Importantly, the CIS^{Sc} 'wedges' consist of

150 two copies of Cis11 and one copy of Cis12 (Fig. 2f), resembling the baseplate of Pyocin
151 R2(27). This is in contrast to other previously reported eCIS, whose baseplate wedge comprises
152 only one Cis11/12 component (AlgoCIS, AFP, PVC) and a Cis11 extension forming a cage
153 around the spike (AlgoCIS) (Supplementary Fig. 6) (13,16,25).

154 Out of the 19 predicted open reading frames in the CIS^{Sc} gene cluster (Fig. 2a), nine encoded
155 proteins were present in the final reconstruction, all with atomic models built (Fig. 2b/c).
156 However, we did not detect a density for CisA in our model, suggesting that CisA is not part
157 of purified CIS^{Sc} particles but may interact via a different mechanism. This is also in agreement
158 with mass spectrometry results that indicate the absence of CisA peptides from purified CIS^{Sc}
159 particles (Fig. 2a) (18). We speculate that the purification protocol used to isolate CIS^{Sc}
160 particles for single-particle analysis may not preserve a CIS^{Sc}-CisA interaction, or the
161 interaction is too transient and only occurs under certain growth conditions. To better
162 understand how CisA may mediate CIS^{Sc} function, we set out to further characterize CisA *in*
163 *vivo*.

164 CisA is a bitopic protein

165 Previous bioinformatic analyses (18,19) and Alphafold2 (28) modeling of CisA suggest that
166 CisA consists of a largely unstructured N-terminal region, a transmembrane segment, and a
167 conserved immunoglobulin-like (IgG) domain at the C-terminus (Fig. 3a). To characterize the
168 intracellular localization of CisA, we first generated a strain in which *cisA* was fused to the N-
169 terminus of *mCherry* and expressed *in trans* from a constitutive promoter in the
170 *S. coelicolor* Δ*cisA* mutant. Using fluorescence light microscopy, we consistently observed a
171 CisA-mCherry fluorescence signal along the hyphal periphery, indicative of a membrane-
172 associated protein (Fig. 3b). In contrast, no fluorescence was observed in WT hyphae carrying
173 an empty plasmid (Fig. 3c). Next, we tested if CisA is indeed localized to the membrane *in*
174 *vivo* by performing cellular fractionation experiments. We separated soluble proteins from
175 membrane proteins using whole cell lysates from the *S. coelicolor* WT or the Δ*cisA* mutant that
176 was complemented with a *cisA-3xFLAG* fusion expressed *in trans* from a constitutive
177 promoter. Our analysis confirmed that CisA-3xFLAG co-sedimented with the cell membranes,
178 while the cytoplasmic transcription factor WhiA could only be detected in the soluble protein
179 fraction (Fig. 3d).

180 Next, we investigated the topology of CisA in the membrane using a dual *phoA-lacZα* reporter
181 system in *E. coli*. The reporter activity can be directly visualized on indicator plates based on
182 the complementary activities of the cytoplasmic reporter β-galactosidase LacZ (magenta
183 coloration) and the periplasmic reporter alkaline phosphatase PhoA (blue coloration) (29). We
184 engineered *E. coli* strains that expressed a C-terminal fusion of CisA variants to the PhoA-
185 LacZα reporter, including full-length CisA and CisA variants that carried either a deletion in
186 the predicted transmembrane domain and/or the putative periplasmic domain (Fig. 3e). In
187 addition, we included three controls, including 1) cells carrying the empty reporter plasmid,
188 resulting only in cytoplasmic β-galactosidase activity, 2) cells expressing a PhoA/LacZ fusion
189 to the *Streptomyces* cytoplasmic cell division protein SepH, and 3) cells expressing a
190 PhoA/LacZ fusion to the periplasmic domain of the *Streptomyces* membrane protein RsbN
191 (30,31). The results of this assay confirmed that CisA is a bitopic protein with an N-terminus
192 (amino acids 1-285) located in the cytoplasm and a C-terminus (amino acids 310-468) present
193 in the periplasm of *E. coli* (Fig. 3f).

194 Collectively, our results demonstrate that CisA is a membrane protein comprised of a flexible,
195 cytoplasmic N-terminal domain and a C-terminal globular IgG-like domain that is exposed to
196 the outside of the cytoplasmic membrane.

197 CisA is essential for the cellular function of CIS^{Sc}

198 We previously established a fluorescence-based assay to demonstrate that the production of
199 functional CIS^{Sc} particles results in a significantly reduced viability of *Streptomyces* hyphae
200 exposed to exogenous stress, including treatment with the membrane-pore forming antibiotic
201 nisin, UV radiation or the protonophore carbonyl cyanide 3-chlorophenylhydrazone (CCCP)
202 (18). This viability assay is based on the measurement of the ratio of two fluorescent markers,
203 namely cytoplasmic sfGFP produced by viable intact hyphae and the membrane dye FM5-95
204 to detect intact as well as partially lysed hyphae. Using this assay, we tested whether CisA was
205 essential for CIS^{Sc}-mediated cell death. We therefore determined the relative viability of the
206 WT *cisA*, the Δ*cisA* and the complemented *cisA* (Δ*cisA/cisA*$^{+}$) strains expressing cytosolic
207 sfGFP. We compared cells exposed to a sublethal concentration of nisin (1 µg/ml for 90 min)
208 to cells not exposed to antibiotic stress. All three strains were found to express CIS^{Sc} assemblies
209 under these growth conditions (Supplementary Fig. 7).

210 Without nisin stress, all three strains exhibited a similar sfGFP/FM5-95 ratio, indicating no
211 significant difference in viability (Fig. 4a/c). As previously observed (18), the viability of the
212 WT was dramatically reduced in response to nisin stress. In contrast, the viability of Δ*cisA*
213 hyphae was unaffected by nisin stress and comparable to the viability of untreated cells. This
214 phenotype could be completely reversed by complementing the Δ*cisA* deletion *in trans* (Fig.
215 4b/d). Notably, the Δ*cisA* strain phenocopies CIS^{Sc} knockout and non-contractile mutants we
216 analyzed previously (18). Thus, we conclude that CisA is required for CIS^{Sc}-mediated cell
217 death upon stress.

218 To further test the dependence of CIS^{Sc} function on CisA, we conducted additional *in vivo*
219 assays. Previous studies showed that the absence of functional CIS^{Sc} impacted the timely
220 differentiation of *Streptomyces* hyphae into chains of spores, resulting in accelerated cellular
221 development and reduced secondary metabolite production (18,19). Here we repeated these
222 analyses using the WT, the Δ*cisA* mutant and the complemented mutant (Δ*cisA/cisA*$^{+}$). All
223 strains consistently completed their life cycle and synthesized spores after 96 h of growth on
224 solid medium (Fig. 4e). Importantly, unlike the WT and the Δ*cisA/cisA*$^{+}$ strain, Δ*cisA* mutant
225 colonies sporulated markedly earlier (72 h). These findings were further corroborated by
226 quantifying the number of spores produced by each strain under the same experimental
227 conditions (Fig. 4f). Finally, we also tested the production of the two characteristic pigmented
228 secondary metabolites of *S. coelicolor*, actinorhodin (blue) (32) and undecylprodigiosin (red)
229 (33). Compared to the WT and the Δ*cisA/cisA*$^{+}$ strain, the Δ*cisA* mutant showed significantly
230 reduced levels of secondary metabolite production (Supplementary Fig. 8). Our data therefore
231 support the conclusion that the cellular function of CIS^{Sc} in *S. coelicolor* depends on CisA, and
232 its absence impacts the timely cellular and chemical differentiation of *S. coelicolor* hyphae.

233 # Discussion

234 Here, we identify CisA as an essential membrane-associated factor that mediates the cellular
235 function of CIS^{Sc} particles in *Streptomyces coelicolor*. In the absence of CisA, CIS^{Sc} are not
236 able to contract in the cellular context (Fig. 1). Similar to a CIS^{Sc} deletion or non-contractile
237 mutant (18), this decreases the induction of cell death upon stress, which in turn affects cellular
238 development and secondary metabolite production (Fig. 5). The mechanistic aspects of this
239 distinct mode of action of a CIS are discussed below.

240 A conserved feature of all previously studied CIS is the requirement of the contractile apparatus
241 to bind to a membrane before firing. This can be achieved in different ways, leading to the
242 classification of CIS into different modes of action. First, T6SS are anchored to the cytoplasmic
243 membrane of the host cell by a trans-envelope complex spanning from the cytoplasm to the
244 inner membrane, periplasm, and outer membrane (34–36). Second, contractile phages and eCIS
245 bind to the surface of their target cell via tail fibers, which are typically connected to the
246 baseplate and transmit the signal for firing to the baseplate (13,16,37). Third, tCIS are anchored
247 to thylakoid membrane stacks in cyanobacteria by an extension of their baseplate (38). Finally,
248 and in contrast to the previously described CIS, we show that intracellular CIS^{Sc} particles from
249 *Streptomyces* do not include structural components that can directly bind the host membrane.
250 Our data suggest that CisA may be required to mediate an interaction of CIS^{Sc} with the
251 cytoplasmic membrane prior to firing (Fig. 5). This interaction may occur directly via the
252 binding of the CIS^{Sc} particle to the membrane protein CisA, or through the interaction with a
253 yet unknown factor. To explore this idea, we performed an *in silico* prediction of protein-
254 protein interactions between monomeric CisA and CIS^{Sc} components using Alphafold2-
255 Multimer (39) (Supplementary Fig. 9a). Interestingly, this analysis identified the baseplate
256 component Cis11 as a significant hit and possible interaction partner of CisA (Supplementary
257 Fig. 9b-d). Importantly, such a protein-protein interaction would be consistent with our
258 cryoEM structure (Fig. 2b-f), showing a peripheral surface-exposed position of Cis11 in the
259 baseplate complex of extended CIS^{Sc}.

260 Additional structural modelling using AlphaFold2-Multimer with truncated versions of CisA
261 in complex with Cis11 further support the idea that the largely unstructured cytosolic portion
262 of CisA is required to interact with the Cis11 (Supplementary Fig. 10). We have been unable
263 to confirm a direct interaction between CisA and Cis11 because the expression of *cisA* is toxic

264 in *E. coli,* which prevented the experimental analysis of the CisA-Cis11 interaction using co-
265 purification approaches and bacterial two-hybrid studies. However, we did detect CisA
266 peptides in crude purifications of CIS^{Sc} from nisin-stressed cells (Supplementary Table 2). This
267 would be consistent with a transient and/or short-lived interaction of CIS^{Sc} particles with CisA,
268 triggered by an exogenous or cellular signal. In agreement with this idea, we rarely observed
269 extended CIS^{Sc} assemblies associated with the cytoplasmic membrane via their baseplate in
270 WT cells (Fig. 1d).

271 We further speculate that CisA may not only serve as a mediator for the interaction of CIS^{Sc}
272 with the cytoplasmic membrane but also as a sensor and checkpoint for inducing cell death
273 only under specific stress conditions or in response to cellular signals. The CisA C-terminal
274 IgG-like domain that is localized outside the cytoplasm and in proximity of the Gram-positive
275 cell wall may sense stress signals that could potentially trigger conformational changes in CisA,
276 which in turn could mediate the recruitment of CIS^{Sc} assemblies to the cytoplasmic membrane,
277 followed by firing. The fatal outcome of firing for the producing cell may have driven the
278 evolution of a stepwise mechanism involving a checkpoint that prevents self-inflicted cell death
279 by accidental firing. Such a mechanism would keep the CIS^{Sc} in a free-floating, non-functional
280 and safe state in the cytoplasm.

281 # METHODS

282 ## Bacterial strains, plasmids, and oligonucleotides

283 Bacterial strains, plasmids, and oligonucleotides used in this study are listed in Supplementary
284 Tables 3-4. Plasmids were generated using either standard restriction-ligation or assembled
285 using the Gibson Assembly Master Mix (NEB) or *In Vivo* Assembly. All plasmids were
286 verified by DNA sequencing. *Escherichia coli* strains were cultured in LB, SOB, or DNA
287 medium. *E. coli* strains TOP10, DH5α and NEB5α were used to propagate plasmids and
288 cosmids, *E. coli* strain BW25113/pIJ790 for recombineering cosmids and *E. coli*
289 ET12567/pUZ8002 for interspecies conjugation. When required, media was supplemented
290 with antibiotics at the following concentrations: 100 µg/ml carbenicillin, 50 µg/ml apramycin,
291 50 µg/ml kanamycin, 50 µg/ml hygromycin.

292 *Streptomyces coelicolor* strains were cultivated in LB, TSB, TSB-YEME, or R2YE liquid
293 medium at 30 °C in baffled flasks or flasks with springs, at 250 rpm or grown on LB, SFM,
294 R2YE medium solidified with 1.5 % (w/v) Difco agar (40). Antibiotics were added at the
295 following concentrations: 25 µg/ml apramycin, 50 µg/ml kanamycin, 25 µg/ml hygromycin,
296 12.5 µg/ml nalidixic acid.

297 ## Construction of the *S. coelicolor* Δ*cisA* mutant

298 The λ RED homologous recombination system was used to isolate gene replacement mutations
299 using PCR-directed mutagenesis (ReDirect) of the *S. coelicolor* cosmid StD8A containing the
300 *cis* gene cluster(41),(42). The *cisA* coding sequence (*SCO4242*) was replaced with the
301 *aac3(IV)-oriT* resistance cassette from pIJ773. The mutant cosmid (pSS684) was introduced
302 into *E. coli* ET12567/pUZ8002, followed by conjugation into *S. coelicolor* M145.
303 Exconjugants that had successfully undergone double-homologous recombination were
304 identified by screening for apramycin resistance and kanamycin sensitivity. The deletion of *cisA*
305 was subsequently verified by PCR.

306 ## Sheath preparation of CIS^{Sc}

307 *S. coelicolor* strains were grown in 30 ml TSB, TSB-YEME or R2YE liquid medium for 48 h.
308 Cells were pelleted by centrifugation (7,000 x g, 10 min, 4 °C), resuspended in 5 ml lysis buffer

309 (150 mM NaCl, 50 mM Tris-HCl, 0.5× CellLytic B (Sigma-Aldrich), 1 % Triton X 100, 200
310 µg/ml lysozyme, 50 µg/ml DNAse I, pH 7.4), and incubated for 1 h at 37 °C. Cell debris was
311 removed by centrifugation (15,000 × g, 15 min, 4 °C) and cleared lysates were subjected to
312 ultra-centrifugation (150,000 × g, 1 h, 4 °C). Pellets were resuspended in 150 µl resuspension
313 buffer (150 mM NaCl, 50 mM Tris-HCl, supplemented with protease inhibitor cocktail
314 [Roche], pH 7.4). CIS^{Sc} sheath preparations were analyzed by negative stain EM imaging (43)
315 and mass spectrometry at the Functional Genomics Center Zürich.

316 To purify non-contractile CIS^{Sc} particles from *S. coelicolor (*SS393*)*, cleared cell lysates were
317 subjected to ultracentrifugation using a sucrose cushion (20 mM Tris pH 8.0, 150 mM NaCl,
318 50 mM EDTA, 1 % Triton X 100, 50 % [w/v] sucrose) (18). The sucrose cushion alongside 1
319 mm of liquid above and residual bacterial contaminants were removed by centrifugation at
320 15,000 x g. Samples were then subjected to a second round of ultracentrifugation without a
321 sucrose cushion (150,000 × g, 1 h, 4 °C) and resulting cell pellets were resuspended in buffer
322 (50 mM Tris, 150 mM NaCl). These crude samples were then purified further by gradient
323 ultracentrifugation (10 %-50 % continuous gradient made with BIOCOMP gradient master IP
324 model 107 gradient forming instrument) at 100,000 x g for 1 h using a SW55 Ti rotor. The
325 gradient was analyzed in 11 fractions of 500 µl and checked by negative stain EM. The
326 fractions, which contained CIS^{Sc} particles, were pooled and used for further experiments.

327 Negative stain electron microscopy

328 4 µl of purified CIS^{Sc} sheath particles were adsorbed to glow-discharged, carbon-coated copper
329 grids (Electron Microscopy Sciences) for 60 s, washed twice with milli-Q water and stained
330 with 2 % phosphotungstic acid for 45 s. The grids were imaged at room temperature using a
331 Thermo Fisher Scientific Morgagni transmission electron microscope (TEM) operated at
332 80 kV.

333 Mass spectrometry analysis

334 To confirm the presence of predicted CIS^{Sc} components, isolated sheath particles were
335 subjected to liquid chromatography–mass spectrometry analysis (LC–MS/MS). These
336 experiments were conducted at the Functional Genomics Center Zürich. First, the samples were
337 digested with 5 µl of trypsin (100 ng/µl in 10 mM HCl) and microwaved for 30 min at 60 °C.

338 The samples were then dried, dissolved in 20 µl ddH_20 with 0.1 % formic acid, diluted in 1:10
339 and transferred to autosampler vials for liquid chromatography with tandem mass spectrometry
340 analysis. A total of 1 µl was injected on a nanoAcquity UPLC coupled to a Q-Exactive mass
341 spectrometer (ThermoFisher). Database searches were performed by using the Mascot
342 swissprot and tremble_streptomycetes search programs. For search results, stringent settings
343 have been applied in Scaffold (1 % protein false discovery rate, a minimum of two peptides
344 per protein, 0.1 % peptide false discovery rate). The results were visualized by Scaffold
345 software ([Proteome Software Inc.], Version 4.11.1).

346 Protein gel electrophoresis and western blotting

347 For general protein analysis, protein samples were boiled at 95 °C for 5 min and separated by
348 a 4–20% Mini-PROTEAN® TGX Stain-Free™ SDS PAGE (BioRad) or 12 % Tris-Glycine
349 SDS PAGA (Invitrogen) and visualized using InstantBlue Coomassie Protein Stain or
350 ReadyBlue Protein Gel Stain (Sigma Aldrich).

351 For western blotting, cells were grown in biological triplicate for 48 h in TSB, 2 ml aliquots of
352 each culture were pelleted and washed once with 1x PBS. Cell pellets were resuspended in 0.4
353 ml of sonication buffer (20 mM Tris pH 8.0, 5 mM EDTA, 1x EDTA-free protease inhibitors
354 [Sigma Aldrich]) and subjected to sonication at 4.5-micron amplitude for 7 cycles of 15 s on /
355 15 s off. Samples were centrifuged at 17,000 x *g* for 15 min at 4 °C. Protein concentration in
356 cleared cell lysate supernatants was determined by Bradford Assay (Biorad). Equivalent total
357 protein concentrations (1 mg/ml) were assayed using the semi-dry western blot transfer. The
358 gel was transferred to a PVDF membrane (Biorad) and probed with the appropriate antibody
359 diluted in TBS-T or using the iBIND buffer system (Thermo Fisher): Rabbit anti-FLAG
360 ([Sigma Aldrich] F7425, 1:2500), Rabbit anti-WhiA ((44), 1:2500), and Goat Anti-Rabbit-
361 HRP (Abcam Ab6721, 1:5000). To visualize HRP-conjugated antibodies, membranes were
362 incubated with SuperSignal West Femto ECL solution (Thermo Fisher).
363

364

365

366

367 ## Cellular fractionation

368 To fractionate membrane and soluble proteins from *S. coelicolor* (WT, SS576), cells were
369 grown for 48 h in 50 ml TSB/YEME and harvested by centrifugation. Cell pellets were
370 resuspended in 1/10 volume of lysis buffer (0.2 M Tris-HCl, pH 8, 10 mg/mL lysozyme, and
371 1× EDTA-free protease inhibitors; [Roche]), incubated for 30 min at 37 °C, and then briefly
372 cooled on ice before lysed by sonication (11 x 15 sec on/off at 50 % power at 8 microns on
373 ice). Cell debris was removed by centrifugation at 16,000 × g for 20 min and supernatant was
374 subsequently subjected to two additional rounds of centrifugation. The cleared cell lysate was
375 subjected to ultracentrifugation for 1 h at 150,000 × g at 4 °C to separate the soluble proteins
376 from membrane proteins. Sedimented membrane proteins were resuspended and washed twice
377 in 1 volume of wash buffer (60 mM Tris-HCl, 200 mM NaCl, pH 8, 0.2 mM EDTA, and 0.2
378 M sucrose) at 150,000 × g at 4 °C for 1 h. The wash step was repeated one final time with the
379 wash buffer containing 8 M urea to remove traces of membrane-associated proteins (45). The
380 final pellet was dissolved in 1/10 of the initial volume with wash buffer (no urea). Equi-volume
381 amounts of fractions were mixed with 2x SDS sample buffer and analyzed by immunoblotting.

382 ## Membrane protein topology analysis in *E. coli*

383 The coding sequence of CisA was inserted in the dual pho-lac reporter plasmid pKTop, which
384 consists of an *E. coli* alkaline phosphatase fragment $PhoA_{22-472}$ fused in frame after the α-
385 fragment of β-galactosidase $LacZ_{4-60}$ (Supplementary Table 3) (29). For membrane protein
386 topology, *E. coli* TG1 was transformed with the pKTop and derivatives. Membrane protein
387 topology was assayed by plating the resulting reporter strains on dual-indicator plates
388 containing LB agar supplemented with 80 µg/ml 5-bromo-4-chloro-3-indolyl phosphate
389 disodium salt (X-Phos) ([Sigma Aldrich], RES1364C-A101X) and 100 µg/mL 6-chloro-3-
390 indolyl-β-d-galactoside (Red-Gal) ([Sigma Aldrich], B6149) as indicators, 1 mM IPTG, and
391 50 µg/ml kanamycin. A periplasmic or extracellular location of the reporter fusion results in
392 higher alkaline phosphatase activity (blue color), whereas a cytosolic location of the reporter
393 leads to higher β-galactosidase activity (magenta color). Plates were incubated for two days at
394 37 °C and scanned.
395

396

397 ## Vitrified sample preparations

398 For single-particle cryoEM (SPA), the *S. coelicolor* non-contractile CIS particles were purified
399 as described above and vitrified using a Vitrobot Mark IV (Thermo Fisher Scientific). 4 µl of
400 samples were applied twice on glow-discharged 200 mesh Quantifoil copper grids (R 2/2)
401 which were manually coated with a layer of 1 nm carbon. Grids were blotted for 5.5 s and
402 plunge-frozen in liquid ethane-propane mix (37 %/63 %). Frozen grids were stored in liquid
403 nitrogen until loading into the microscope.

404 For cryo-electron tomography (cryoET), *Streptomyces* cells were mixed with 10 nm Protein A
405 conjugated colloidal gold particles (1:10 v/v, [Cytodiagnostics]) and 4 µl of the mixture was
406 applied to a glow-discharged holey-carbon copper EM grid (R2/1 or R2/2, [Quantifoil]). The
407 grid was automatically blotted from the backside for 4-6 s in a Mark IV Vitrobot by using a
408 Teflon sheet on the front pad, and plunge-frozen in a liquid ethane-propane mixture (37 %/63
409 %) cooled by a liquid nitrogen bath.

410 ## SPA data collection and image processing

411 44,925 movies were collected on Titan Krios microscope (Thermo Fisher Scientific), operated
412 at 300 keV equipped with K3 direct electron detector, operating in counting mode, and using
413 a slit width of 20 eV on a GIF-Quantum energy filter (Gatan). The automated data collection
414 was conducted with EPU software (Thermo Fisher Scientific) with a final pixel size of
415 1.065Å/pix over 40 frames with a total dose of 50 $e^-/Å^2$. The targeted defocus was set between
416 -1.6 and -2.8 µm with 0.2 µm increment.

417 Movie-alignments with dose-weighting were performed in MotionCor2 software (46) with a
418 gain reference estimated a posteriori (47) followed by standard in-house pipeline of manual
419 inspection and selection of 38,845 micrographs (48) for further processing in cryoSPARC
420 package v4.0.3 (49). Due to the low concentration of particles and the presence of other
421 contaminants in the sample, automatic particle picking appeared challenging, and we
422 developed CIS-specific approach for efficient picking of the cap and baseplates. In this
423 approach, CIS^{Sc} particles were manually selected as filaments (start-to-end) on 920
424 micrographs and used for training a crYOLO (50) picking model (Supplementary Fig. 2). The
425 large size of the training set appeared essential for successful picking; we could not get rid of
426 large number of false-positive picks, but there were not so many false-negative picks. Then,

427 CIS^{Sc} particles were picked in crYOLO as filaments, followed by the extraction of the ends of
428 the "filaments" using star_modif.py script (48). Particle coordinates were imported in
429 cryoSPARC, where 211,041 particles were extracted at a large box size of 756 pixels binned
430 to 64 pixels for initial 2D-classification, which allowed us to separate initial particle sets
431 corresponding to the CIS^{Sc} cap (36,569 particles) and CIS^{Sc} baseplate (43,087 particles)
432 (Supplementary Fig. 2).

433 Two subsets of this dataset were processed in cryoSPARC separately. For the cap subset, a
434 standard cryoSPARC single-particle processing approach was applied, including gradual
435 iterative 2D-classification rounds, followed by selection of good classes and particle re-
436 extraction at finer sampling. The main challenge was the proper centering of the particles
437 selected on the end of elongated filament-like objects with repeating patterns (sheath-tube
438 module of CIS), hampering the alignments. Ab-initio model generation with applied C6
439 symmetry was hampered by poor centering of 2D-classes due to elongated nature of the
440 particles (Supplementary Fig. 2). Homo-refinement with this reference was performed
441 followed by particle re-extraction and one more round of ab-initio model generation with
442 applied C6 symmetry (Supplementary Fig. 2). The new 3D-reconstruction appeared reliable
443 and was used for further iterative 3D-refinements (Homo-refinement and NU-refinements)
444 accompanied by 2D-classification and CTF-refinement rounds to exclude particles with wrong
445 Euler angle assignments. The final 3.4 Å resolution map with imposed C6 symmetry resulted
446 from 19,218 particles.

447 The baseplate subset was processed using the same approach, resulting in a 3D-reconstruction
448 with imposed C6 symmetry with a resolution of 3.5Å from 22,980 particles (Supplementary
449 Fig. 2). The tip of the baseplate has a C3 symmetry, therefore to solve that part of the map
450 correctly, we exported that particle stack to Relion4 (51) and took advantage of 2D-
451 classification in Relion to select 18,124 particles, corresponding to the best 2D classes
452 averages. 3D-refinement with relaxed symmetry resulted in a 3.8 Å 3D-resolution
453 reconstruction with imposed C3 symmetry.

454 Cryo-electron tomography

455 Intact *Streptomyces* cells were imaged by cryoET as described previously (52). Images were
456 recorded using a Titan Krios 300 kV microscope (Thermo Fisher Scientific) equipped with a
457 Quantum LS imaging filter operated at a 20 eV slit width and with K3 Summit direct electron

458 detectors (Gatan). Tilt series were collected using a bidirectional tilt-scheme from -60 to +60°
459 in 2° increments. Total dose was 130-150 $e^-/Å^2$ and defocus was kept at -8 µm. Tilt series were
460 acquired using SerialEM (53), drift-corrected using alignframes, and reconstructed using
461 IMOD program suite (54). To enhance contrast, tomograms were deconvolved with a Wiener-
462 like filter 'tom_deconv' (55).

463 Structural modeling of the CIS^{Sc} complex

464 The map qualities of different modules of CIS^{Sc} (cap and baseplate) allowed for *de novo*
465 structural modelling (Supplementary Fig. 2-3). The atomic models of SCO4243-4248,
466 SCO4252-4253 and SCO4260 were built *de novo* using COOT (56). The resulting models were
467 iteratively refined using RosettaCM (57) and real-space refinement implemented in PHENIX
468 (58). In cases where protein domains could only be partially modeled, side chains were not
469 assigned. Final model validation was done using MolProbity (58) and correlation between
470 models and the corresponding maps were estimated using mtriage (58). To illustrate the
471 complete CIS^{Sc} structure, we generated a composite model by integrating symmetry-related
472 protein subunits into a full model of the CIS^{Sc}, based on the consistent CIS^{Sc} length observed
473 both *in situ* and *in vitro* (Fig. 2b).

474 Fluorescence microscopy

475 Fluorescence-based cell viability assays were performed as described previously (18). Briefly,
476 to produce cytoplasmic sfGFP in *Streptomyces*, the coding sequence for sfGFP was introduced
477 downstream of the constitutive promoter *ermE** on an integrating plasmid. The plasmid was
478 introduced by conjugation to *S. coelicolor* strains (SS430, SS575, SS576. An equal level of
479 cytoplasmic sfGFP in the different strains was confirmed by Western blotting (Supplementary
480 Fig. 11). *Streptomyces* strains were grown in 30 ml of TSB liquid culture at 30 ˚C with shaking
481 at 250 rpm for 48 h. Where appropriate, nisin was added to a final concentration of 1 µg/ml 90
482 min prior to imaging. One ml aliquots of each culture were centrifuged for 5 min at 15,000 x
483 *g*, washed twice with 1xPBS, resuspended in 1 ml of 1xPBS containing 5 µg/ml of the red-
484 fluorescent membrane dye FM5-95 (Invitrogen) and then incubated in the dark at room
485 temperature for 10 min followed by two wash steps with 1x PBS. Washed cell pellets were
486 resuspended in a total volume of 50 µl PBS and 10 µl of each sample was spotted onto 1 %
487 agar pads and subsequently imaged using the Thunder imager 3D cell culture microscope

488 (Leica). First, tile scan images were acquired using the Las X Navigator plug-in software (Leica
489 Application Suite X, Version 3.7.4.23463), and 100 regions of interest were picked manually.
490 Then Z-stack images were acquired using a HC PL APO 100x objective with the following
491 excitation wavelengths: GFP (475 nm) and TRX (555 nm). Images were processed using LasX
492 software to apply thunder processing and maximum projection and FIJI to create segmentation
493 and quantify the live (sfGFP)/total cells (FM5-95) area ratio (59). Statistical analyses were
494 performed on data from biological triplicates (n=100 images for each experiment) using a one-
495 way ANOVA and Tukey's post-test in GraphPad Prism 9 (Version 9.3.1).

496 For imaging the subcellular localization of the CIS adaptor protein in *Streptomyces*, cells (strain
497 JS69 or *S. coelicolor* M145) were grown for 48 h in TSB/YEME liquid medium. Two µl of
498 each strain were spotted on 1 % agarose pads and subsequently imaged. Images were acquired
499 using a Zeiss Axio Observer Z.1 inverted epifluorescence microscope fitted with a sCMOS
500 camera (Hamamatsu Orca FLASH 4), a Zeiss Colibri 7 LED light source, and a Hamamatsu
501 Orca Flash 4.0v3 sCMOS camera. mCherry fluorescence was detected using an
502 excitation/emission bandwidth of 577–603 nm/614–659 nm. Images were collected using Zen
503 Blue (Zeiss) and analyzed using Fiji (59).

504 Cover glass impression of *Streptomyces* spore chains

505 Spore titers of relevant strains were determined by dilution plating (18). 10^7 colony forming
506 units (CFU) of *S. coelicolor* strains (WT, SS539, SS557) were spread onto R2YE agar plates
507 and grown at 30 °C. Sterile glass coverslips were gently applied to the top surface of each
508 bacterial lawn after 48 h, 72 h and 96 h post inoculation. Coverslips were then mounted onto
509 glass microscope slides and imaged using a 40x objective on a Leica Thunder Imager 3D Cell
510 Culture. Images were processed using FIJI (59).

511 Actinorhodin production assay

512 *S. coelicolor* strains (WT, SS539, SS557) were inoculated into 30 ml R2YE liquid media at a
513 final concentration of 1.5 x 10^6 CFU/ml. Cultures were grown in baffled flasks at 30 °C
514 overnight. Cultures were standardized to an OD_{450} of 0.5 and inoculated in 30 ml of fresh R2YE
515 liquid medium. For visual comparison of pigment production, images of the growing culture
516 were taken between t = 0 and t = 72 h (as indicated in Supplementary Fig. 7). For quantification

517 of total actinorhodin production, 480 µl of samples were collected at the same time points
518 where images were taken. 120 µl of 5M KOH was added, samples were vortexed and
519 centrifuged at 5,000 x *g* for 5 min. The weight of each tube was recorded. A Synergy 2 plate
520 reader (Biotek) was used then to measure the absorbance of the supernatant at 640 nm. The
521 absorbance was normalized by the weight of the wet pellet.

522 Structure prediction and in silico protein-protein interaction screen

523 CisA structure was predicted using AlphaFold2 (28) and further processed using UCSF
524 Chimera (60) or ChimeraX-1.7.1 (61).

525 A pairwise *in silico* screen for possible interactions between CisA and components encoded
526 by the *S. coelicolor cis* gene cluster (*SCO4242-SCO4260*) was conducted using the AlphaFold2
527 Multimer-based LazyAF pipeline (28,39,62). The confidence metric (ipTM) for the top model
528 from each pairwise interaction was tabulated and visualised using Prism (Version 10.2.2) with
529 ipTM scores >0.7, indicating a possible protein-protein interaction (63).
530

531 Bioinformatic analysis of CisA homologs

532 To identify CisA homologs, we performed a reciprocal BLAST search in 120 genomes of
533 *Streptomyces* and other *Actinomycete* species that were previously reported to include a type
534 IId eCIS (8,19) using the closely related *cisA* homologue from *Streptomyces albus* J1074
535 (YP_007743954.1) as a query (72% identical to CisA from *S. coelicolor*) (Supplementary Data
536 1). Of these 120 genomes, 75 had a reciprocal hit for CisA (Supplementary Data 2). Protein
537 sequences of CisA homologs were aligned using Clustal Omega (64) and visualized with
538 JalView (Version 2.11.3.3).
539

540 Data availability

541 Representative reconstructed tomograms (EMD-50935, EMD-50939, EMD-50940, EMD-
542 50944, EMD-50948, EMD-50949) and SPA cryoEM maps (EMD-51564, EMD-51565 and
543 EMD-51566) have been deposited in the Electron Microscopy Data Bank. Atomic models
544 (PDB: 9GTP, PDB: 9GTR, PDB: 9GTS) have been deposited in the Protein Data Bank.

Acknowledgements

We thank ScopeM for instrument access at ETH Zürich. We thank the Functional Genomics Center Zürich for mass spectrometry support. Pilhofer Lab members are acknowledged for discussions. M.P. was supported by the Swiss National Science Foundation (31003A_179255/310030_212592), the European Research Council (679209), and the NOMIS foundation. Work in the lab of S.S. was supported by a Royal Society University Research Fellowship (URF\R1\180075 and URF\R\231009) and BBSRC grant BB/T015349/1 to S.S. and by the BBSRC Institute Strategic Program grant BB/X01097X/1 to the John Innes Centre.

554 # Author contributions statement

555 B.C., S.S. and M.P. conceived the project. B.C. optimized the sample preparation for SPA;
556 B.C. and P.A. collected and processed the cryoEM data, reconstructed the cryoEM map; B.C.,
557 P.E.H. and J.X. built and refined the structural models; B.C. and P.E.H. conducted and
558 processed cryoET; B.C. conducted automated fluorescent light microscopy, determined
559 sporulation efficiency and actinorhodin production; J.W.S. and S.S. generated plasmids and
560 *Streptomyces* strains; J.W.S. designed constructs and performed membrane topology assay.
561 J.W.S. prepared samples and performed cellular fractionation experiment. J.W.S. imaged
562 strains expressing fluorescently tagged CisA. S.S. and G.C. performed bioinformatic analysis
563 of CisA. B.C., J.W.S., S.S. and M.P. wrote the manuscript.

Competing interests statement

The authors declare no competing interests.

566 **Figures legends**

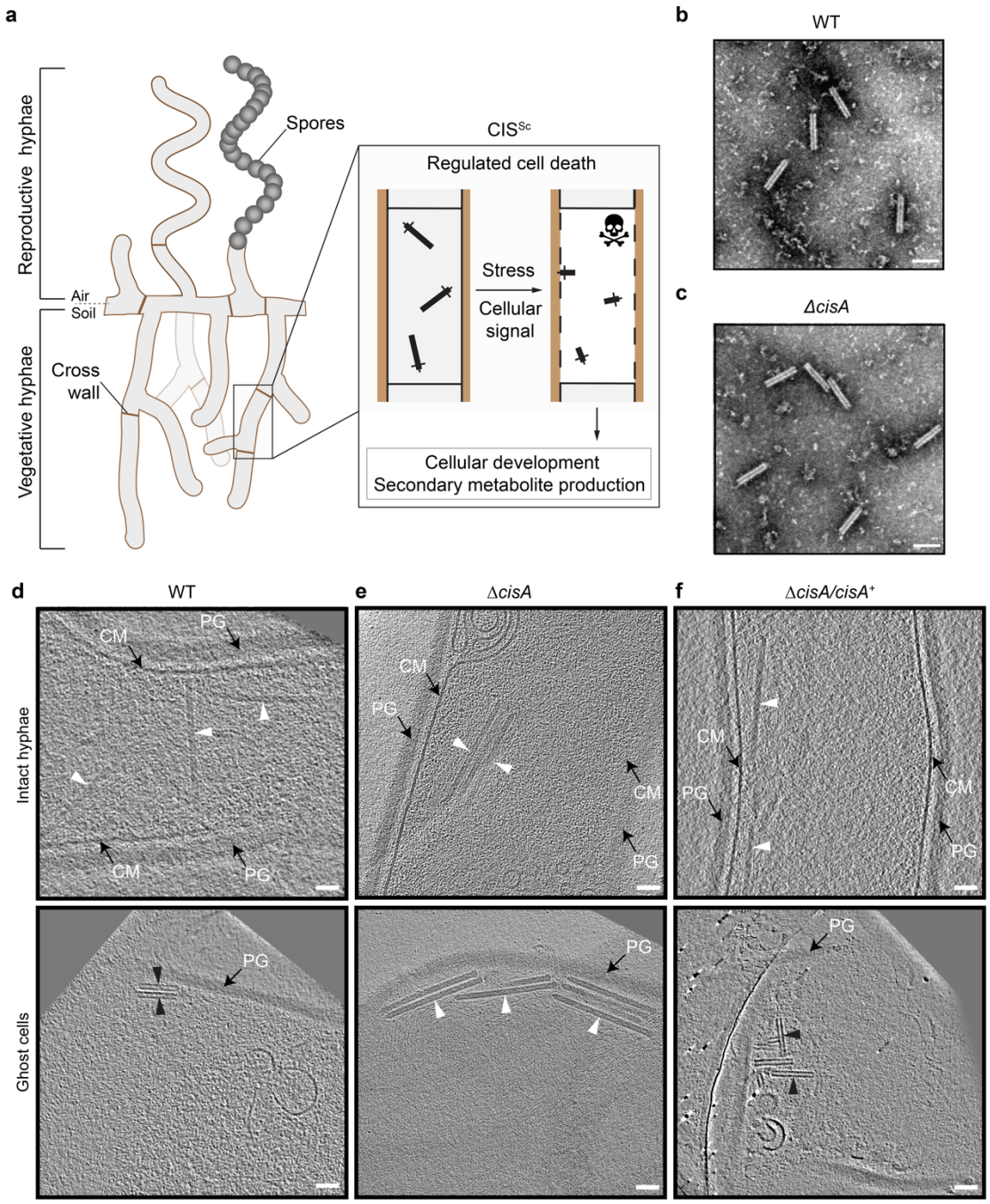

567

568 **Figure 1: Contraction of CIS^{Sc} *in situ* is dependent on CisA.**

569 **a.** Schematic of the mode of action of CIS^{Sc} in *Streptomyces coelicolor* (18,19). CIS^{Sc} are
570 assembled as free-floating particles in the cytoplasm of vegetative hyphae. In response to
571 cellular stress and/or an unknown cellular signal, CIS^{Sc} particles contract, which results in
572 regulated cell death (mediated by released effectors) and impacts cellular development.

573 **b/c.** Negative-stain electron micrographs of purified CIS^{Sc} particles from *S. coelicolor* wildtype
574 (WT) (b) and the Δ*cisA* mutant (c), show that all CIS^{Sc} particles are contracted upon
575 purification. These experiments were performed three independent times. Bars, 100 nm.

576 **d-f.** Shown are representative images of cryo-electron tomogram slices (thickness 11 nm) of
577 vegetative hyphae (top: intact cells; bottom: ghost cells) of *S. coelicolor* WT (d), Δ*cisA* mutant
578 (e), and the complemented Δ*cisA/cisA*$^{+}$ mutant (f). CIS^{Sc} particles remain almost exclusively
579 in an extended state (white arrowheads) in the Δ*cisA* mutant, whereas in ghost cells derived
580 from the WT and the complemented mutant, CIS^{Sc} particles (black arrowheads) are mostly
581 contracted. See also Supplementary Fig. 1. PG, peptidoglycan; CM, cytoplasmic membrane;
582 Bars, 50 nm.

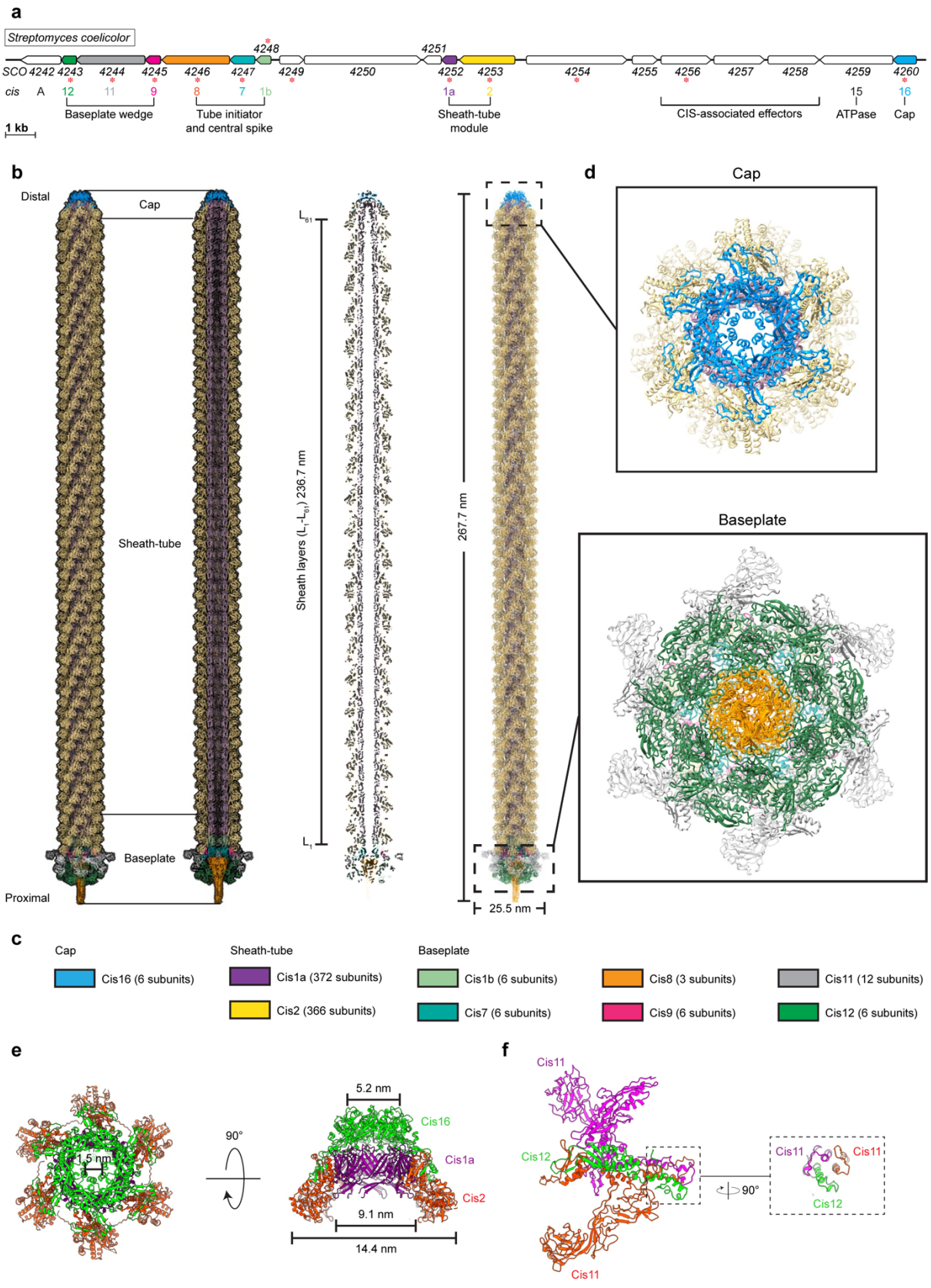
a
Streptomyces coelicolor
SCO 4242 4243 4244 4245 4246 4247 4248 4249 4250 4251 4252 4253 4254 4255 4256 4257 4258 4259 4260
cis A 12 11 9 8 7 1b 1a 2 15 16
Baseplate wedge
Tube initiator and central spike
Sheath-tube module
CIS-associated effectors
ATPase
Cap
1 kb
b
Distal
Cap
Sheath-tube
Baseplate
Proximal
Sheath layers (L1-L61) 236.7 nm
267.7 nm
25.5 nm
d
Cap
Baseplate
c
Cap
Cis16 (6 subunits)
Sheath-tube
Cis1a (372 subunits)
Cis2 (366 subunits)
Baseplate
Cis1b (6 subunits)
Cis7 (6 subunits)
Cis8 (3 subunits)
Cis9 (6 subunits)
Cis11 (12 subunits)
Cis12 (6 subunits)
e
1.5 nm
90°
5.2 nm
Cis16
Cis1a
Cis2
9.1 nm
14.4 nm
f
Cis11
Cis12
90°

583

584

585 **Figure 2: CryoEM structure of the extended CIS^{Sc} assembly reveals its composition.**

586 **a.** Schematic illustrating the CIS^{Sc} gene cluster (adapted from (18)). Asterisks indicate gene
587 products that were detected by mass spectrometry analyzing crude preparations of CIS^{Sc}
588 particles (red). See also Supplementary Table 1.

589 **b/c.** Single-particle cryoEM structure of an extended CIS^{Sc} particle obtained from purified
590 particles from a non-contractile CIS^{Sc} mutant. Shown is the composite atomic model in surface
591 (left) and ribbon (right) rendering (b). Subunits are color-coded according to (a) and their copy
592 numbers in the assembly are indicated in (c).

593 **d.** Perpendicular views of the ribbon representation of the CIS^{Sc} model of the cap and baseplate
594 modules.

595 **e.** Top view (left) and side view (right) of ribbon diagrams showing the cap module of CIS^{Sc},
596 revealing that the cap is composed of a Cis16 hexamer.

597 **f.** Ribbon diagrams showing a single baseplate wedge subunit, which is composed of two
598 copies of Cis11 and one copy of Cis12.

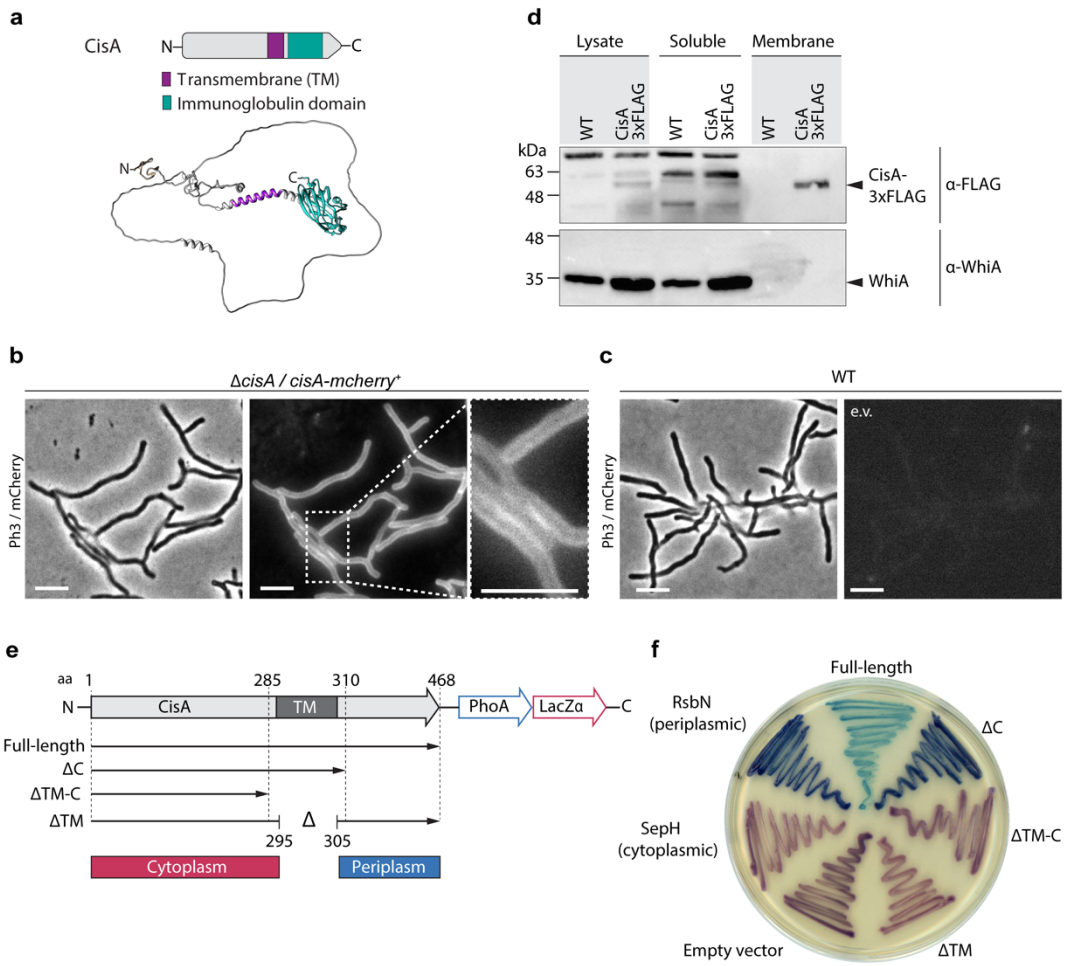

Figure 3: CisA is a single-pass membrane protein.

a. Schematic and Alphafold2 model of CisA. CisA is predicted to contain a largely unstructured N-terminal domain (grey), a transmembrane domain (TM, purple) and a C-terminal immunoglobulin-like domain (green).

b/c. Representative micrographs (left panels: phase contrast, Ph3; right panel: mCherry) of strains of *S. coelicolor* vegetative hyphae either constitutively expressing CisA-mCherry (Δ*cisA/cisA-mcherry*) *in trans* (b) or WT cells carrying an empty vector (e.v.) to control for background fluorescence (c). Box shows a magnified region of hyphae with CisA-mCherry accumulation in the cellular periphery. Bars, 5 µm.

d. Western blot of the cellular fractionation of samples from the *S. coelicolor* WT or the Δ*cisA* mutant constitutively expressing a CisA-3xFLAG fusion *in trans*. Lysate and soluble and membrane fractions were probed for the presence of CisA-3xFLAG with an α-FLAG antibody

612 (top). Fractionation efficiency was assessed using an α-WhiA antibody to detect the soluble
613 transcription factor WhiA (bottom). CisA-3xFLAG was detected in the lysate and the
614 membrane fraction. The experiment was performed in biological duplicates and shown is a
615 representative image.

616 **e/f.** Experimental determination of the CisA membrane topology using the dual *phoA-lacZα*
617 reporter in *E. coli*. The schematic diagram (e) depicts the four CisA constructs used in the assay
618 and indicates the relevant amino acid (aa) deleted in the three CisA mutant derivates. The
619 analysis of colony coloration (f); pink coloration for cytosolic proteins and blue coloration for
620 periplasmic proteins, indicates that the CisA N-terminus is localized in the cytoplasm and the
621 CisA C-terminus localized to the periplasm and this topology is dependent on the
622 transmembrane domain (TM). *E. coli* strains carrying an empty reporter plasmid or reporter
623 plasmids with the *Streptomyces* genes for SepH (cytoplasmic) and RsbN (periplasmic) were
624 used as controls. Note that expression of full-length CisA in *E. coli* is toxic, leading to reduced
625 growth and lighter blue coloration.

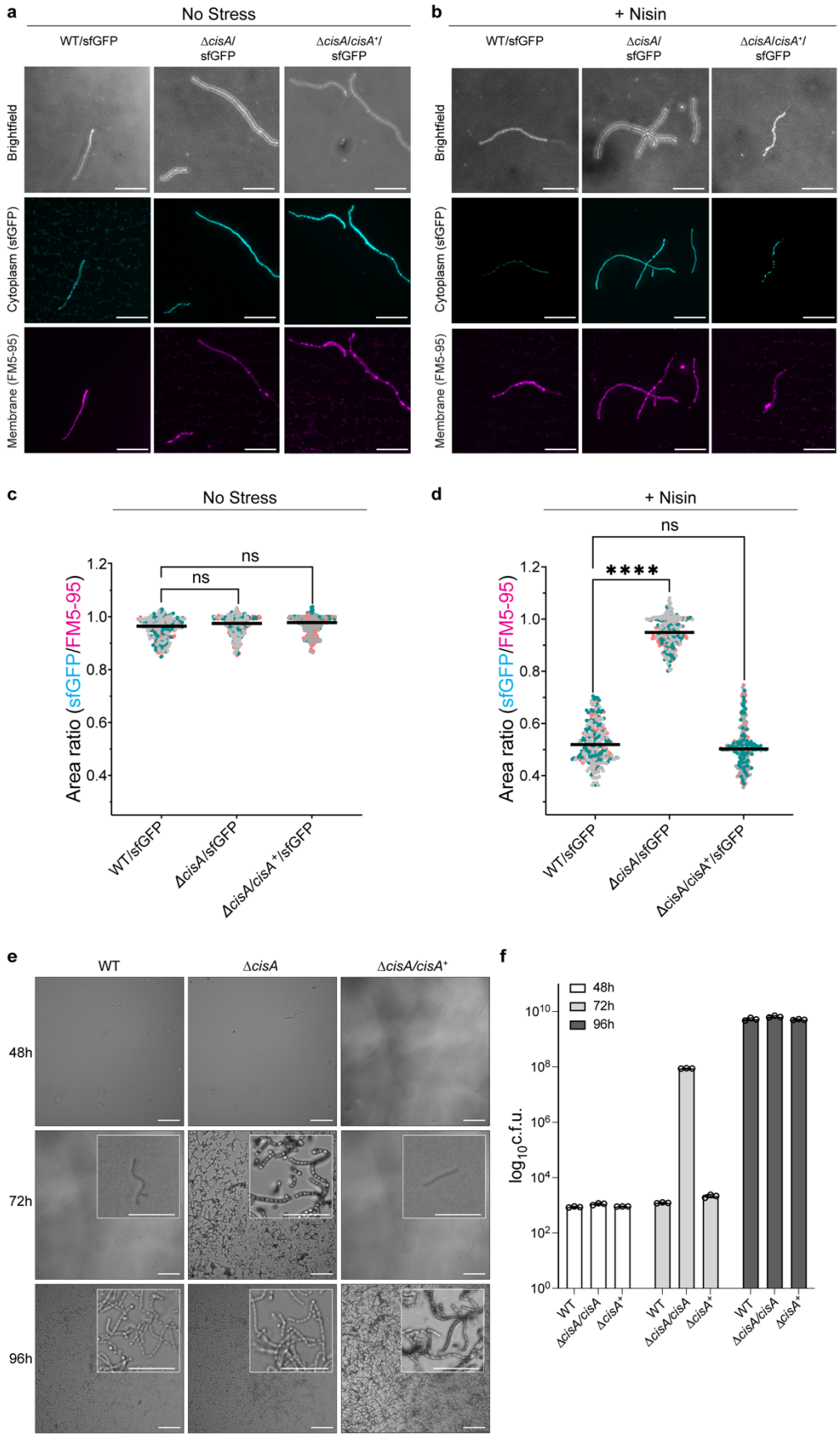
a
No Stress
WT/sfGFP
ΔcisA/ sfGFP
ΔcisA/cisA+/ sfGFP
Brightfield
Cytoplasm (sfGFP)
Membrane (FM5-95)
b
+ Nisin
WT/sfGFP
ΔcisA/ sfGFP
ΔcisA/cisA+/ sfGFP
Brightfield
Cytoplasm (sfGFP)
Membrane (FM5-95)
c
No Stress
ns
ns
Area ratio (sfGFP/FM5-95)
1.2
1.0
0.8
0.6
0.4
WT/sfGFP
ΔcisA/sfGFP
ΔcisA/cisA+/sfGFP
d
+ Nisin
ns
****
Area ratio (sfGFP/FM5-95)
1.2
1.0
0.8
0.6
0.4
WT/sfGFP
ΔcisA/sfGFP
ΔcisA/cisA+/sfGFP
e
WT
ΔcisA
ΔcisA/cisA+
48h
72h
96h
f
48h
72h
96h
log10c.f.u.
10^10
10^8
10^6
10^4
10^2
10^0
WT
ΔcisA/cisA
ΔcisA+
WT
ΔcisA/cisA
ΔcisA+
WT
ΔcisA/cisA
ΔcisA+

626

627 **Figure 4: CisA is required for regulated cell death and cellular function of CIS^{Sc}.**

628 **a-d.** Light microscopy-based viability assay showing that CIS^{Sc} do not mediate cell death in
629 CisA-deficient hyphae in response to exogenous stress. Shown are representative micrographs
630 of the WT/sfGFP, the Δ*cisA*/sfGFP and the complemented Δ*cisA/cisA*$^{+}$/sfGFP mutant
631 expressing cytosolic sfGFP (indicator for live cells). Strains were grown for 48 h and then
632 either incubated without (a) or with (b) the membrane-disrupting antibiotic nisin (1 µg/ml nisin
633 for 90 min). Samples were subsequently stained with the fluorescent membrane dye FM5-95
634 to visualize the cytoplasmic membrane. Bars, 10 µm. Z-stacks were taken of the samples and
635 the relative fluorescence ratio from sfGFP to FM5-95 was calculated in c/d. WT and
636 Δ*cisA/cisA*$^{+}$ complemented cells showed a significantly higher rate of cell death in response to
637 nisin treatment than Δ*cisA* cells. There is no significant difference in the viability of the tested
638 strains in the absence of nisin. Experiments were performed in three biological replicates
639 (green, grey and pink data points). Black lines indicate the mean ratio derived from biological
640 triplicate experiments (n=100 images per replicate). ns (not significant) and **** ($p < 0.0001$)
641 were determined using a one-way ANOVA and Tukey's post-test.

642 **e.** Visualization of spore production in WT, Δ*cisA* mutant and Δ*cisA/cisA*$^{+}$ mutant reveal
643 accelerated cellular development of the Δ*cisA* mutant. Shown are representative brightfield
644 images of surface impressions of plate-grown colonies of each strain taken at the indicated time
645 points. Only sporulating hyphae will attach to the hydrophobic cover glass surface. Insets show
646 magnified regions of the colony surface containing spores and spore chains. Bars, 50 µm.

647 **f.** Quantification of sporulation shown in (e) via counts of colony-forming units (c.f.u.). The
648 graph shows a 6-fold higher c.f.u. count at 72 h in the Δ*cisA* mutant. Strains were grown on
649 R2YE agar and spores were harvested after 48 h, 72 h, and 96 h of incubation. Data show mean
650 ± s.d. obtained from biological triplicate experiments.

651

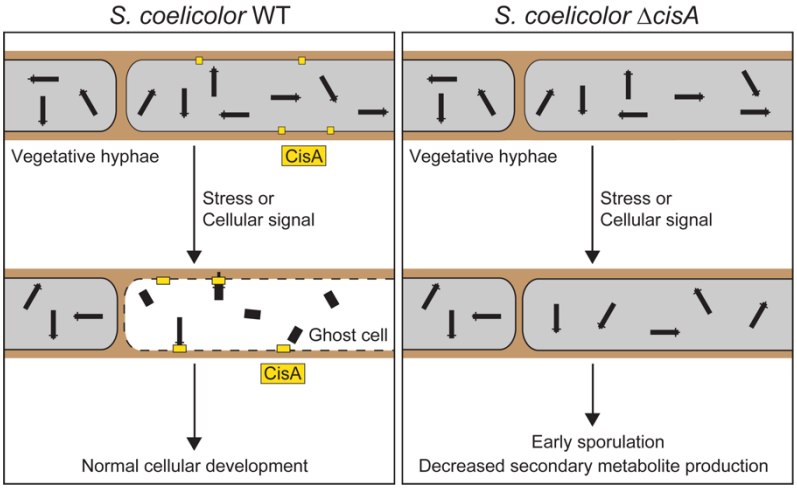

652 **Figure 5: Cytoplasmic CIS^{Sc} require the membrane protein CisA for contraction and**
653 **function.**

654 Proposed model illustrating a possible role of CisA. In response to exogenous stress or an
655 unknown cellular signal, membrane-bound CisA either directly or indirectly mediates the
656 association of free-floating CIS^{Sc} particles with the cytoplasmic membrane, leading to CIS^{Sc}
657 firing and regulated cell death, which impacts the *Streptomyces* developmental life cycle.
658

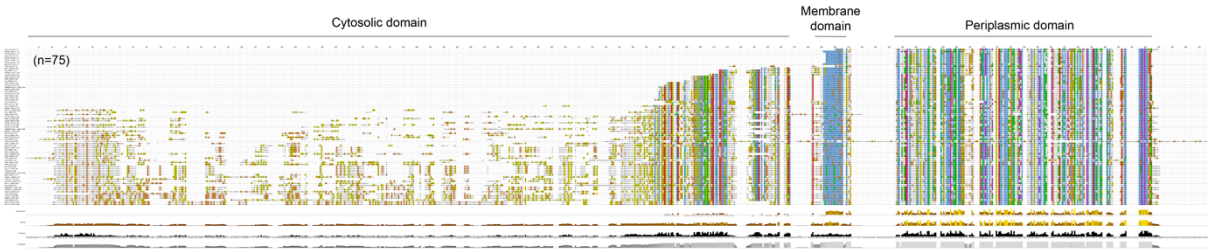

Supplementary Figure 1: CisA is conserved among CIS-positive *Streptomyces* and Actinomycete species.

Protein alignment of CisA homologs identified via reciprocal BLAST search in genomes of Streptomyces and Actinomycete species previously reported to encode an eCIS class IId region. Protein sequences (n=75) were aligned with Clustal Omega and visualized using JalView. CisA domain structure is indicated on top. Genome accession numbers and BLAST results are listed in Supplementary Data 1 and 2.

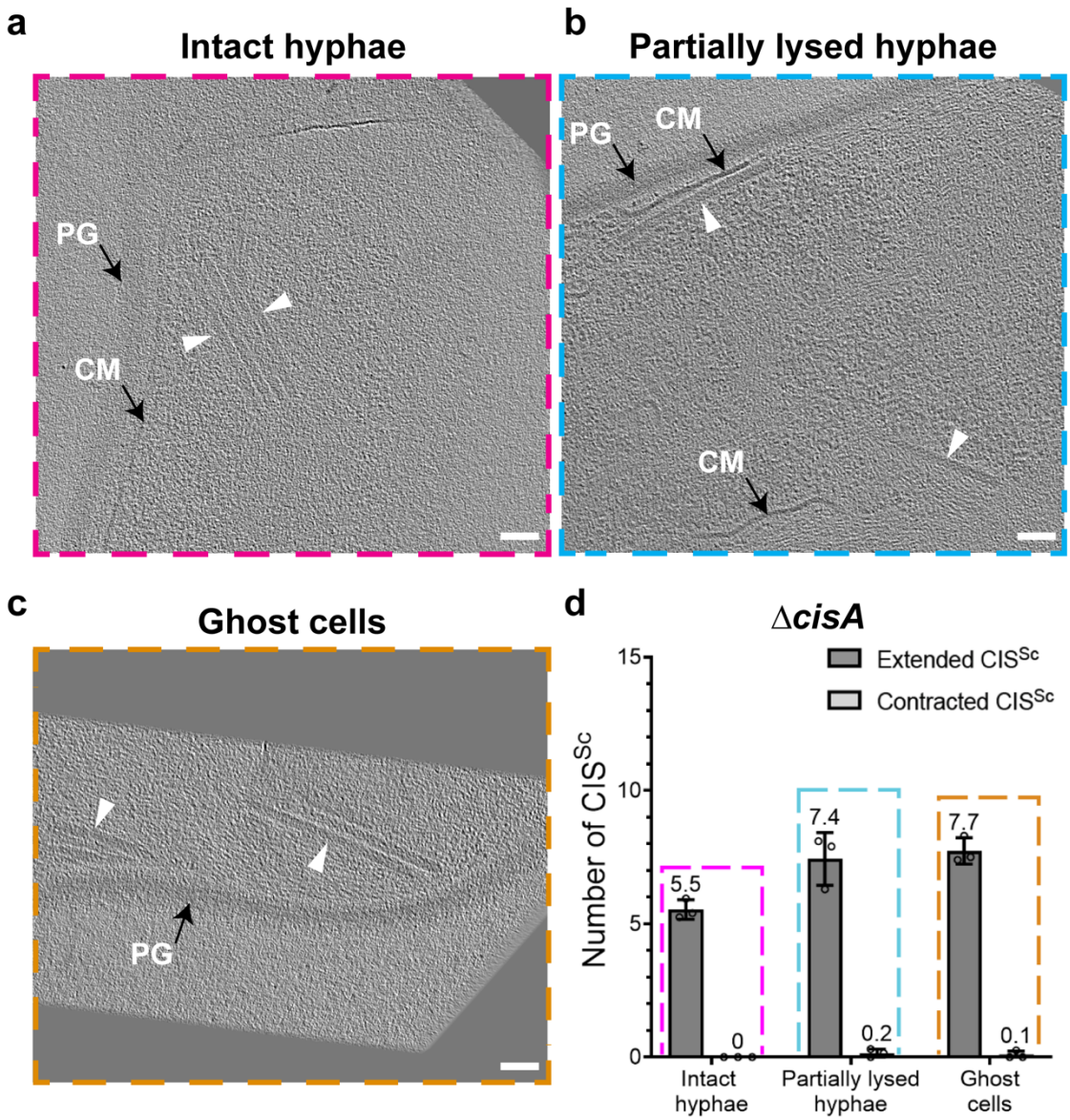

Supplementary Figure 2: Sheath contraction *in situ* is linked to the presence of CisA.

a-c. Shown are additional cryo-tomographic slices (thickness 11 nm) of *S. coelicolor* Δ*cisA* vegetative hyphae, which were observed as 'Intact hyphae' (a), 'Partially lysed hyphae' (b) and 'Ghost cells' (c). Note that all visible CIS^{Sc} particles (white arrowheads) are in the extended conformation. PG, peptidoglycan; CM, cytoplasmic membrane/membranes. Bars, 50 nm.

d. Shown is a quantification of CIS^{Sc} assemblies per tomogram and their conformations as observed in different classes of Δ*cisA* hyphae. Almost all CIS^{Sc} particles were seen in the extended conformation, indicating that sheath contraction *in situ* correlates with the presence of CisA. Data shows mean values and standard deviations obtained from biological triplicate experiments, with n=30 tomograms for each class of hyphae.

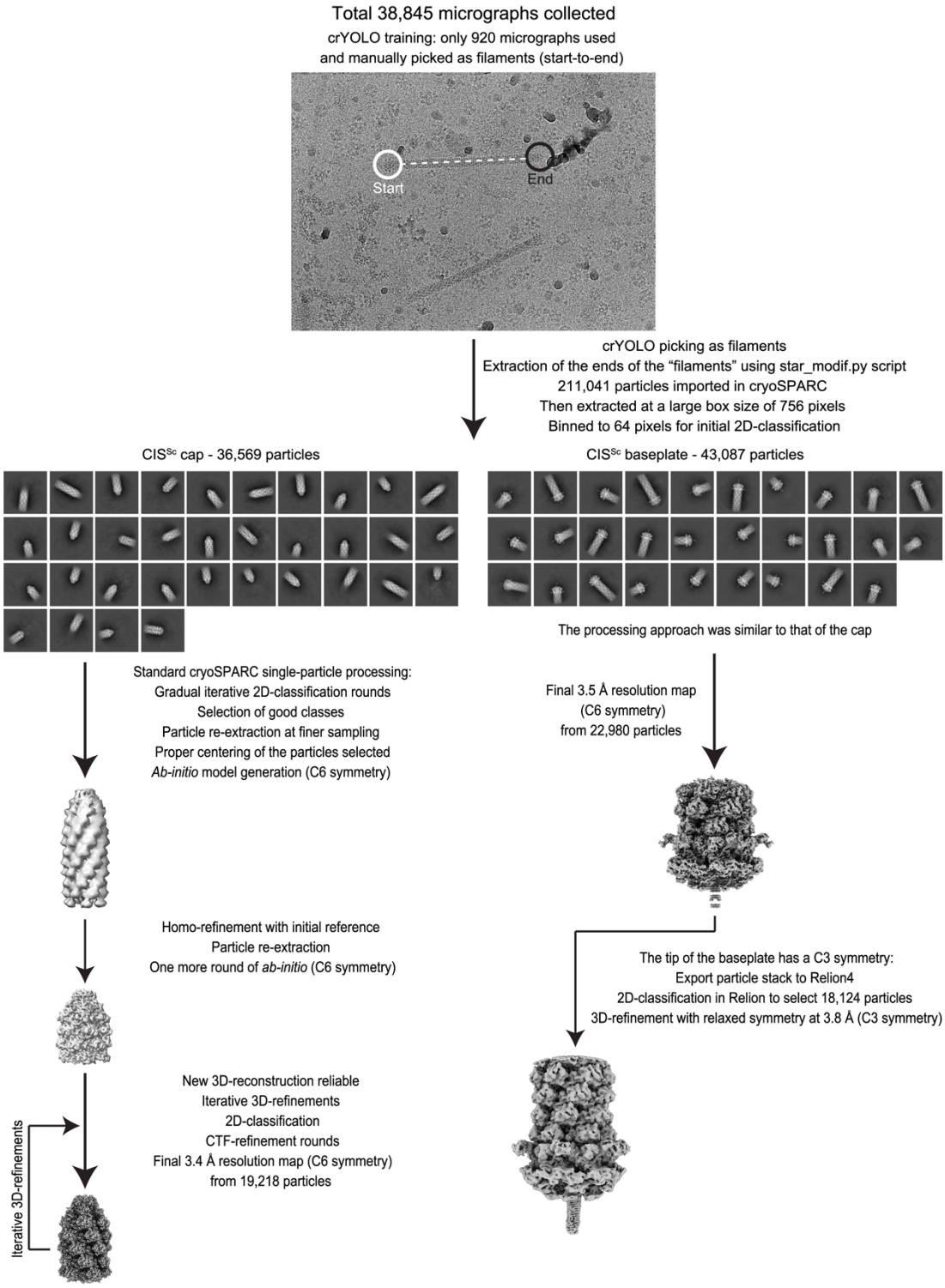

Supplementary Figure 3: Workflow for the cryoEM structural determination of the extended CIS^{Sc}.

Flowchart for cryoEM reconstruction of the extended CIS^{Sc} particle. See METHODS and Supplementary Table 1 for details.

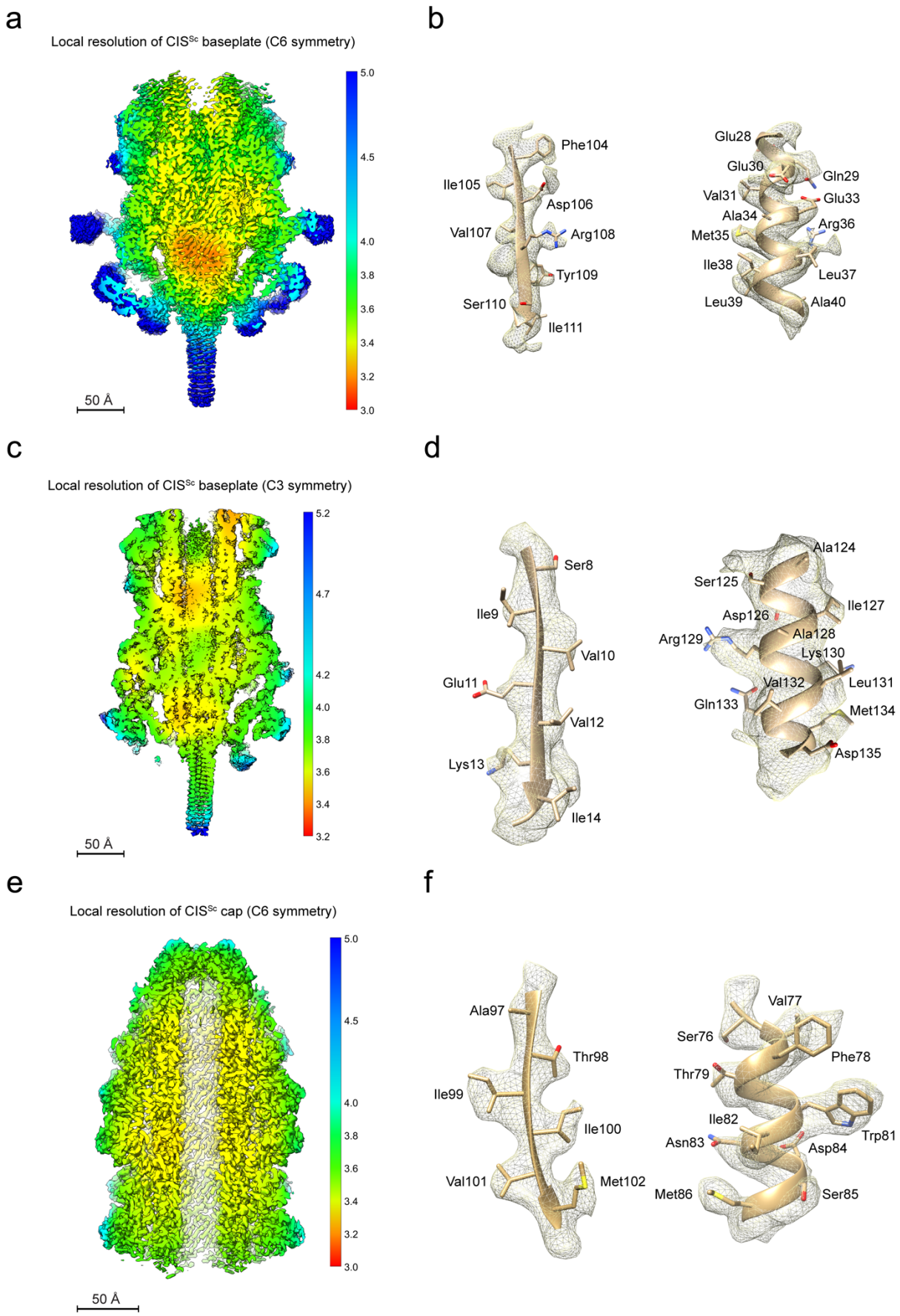
a
Local resolution of CIS^Sc baseplate (C6 symmetry)
5.0
4.5
4.0
3.8
3.6
3.4
3.2
3.0
50 Å
b
Phe104
Ile105
Asp106
Val107
Arg108
Tyr109
Ser110
Ile111
Glu28
Glu30
Gln29
Val31
Glu33
Ala34
Arg36
Met35
Ile38
Leu37
Leu39
Ala40
c
Local resolution of CIS^Sc baseplate (C3 symmetry)
5.2
4.7
4.2
4.0
3.8
3.6
3.4
3.2
50 Å
d
Ser8
Ile9
Val10
Glu11
Val12
Lys13
Ile14
Ala124
Ser125
Ile127
Asp126
Arg129
Ala128
Lys130
Leu131
Val132
Gln133
Met134
Asp135
e
Local resolution of CIS^Sc cap (C6 symmetry)
5.0
4.5
4.0
3.8
3.6
3.4
3.2
3.0
50 Å
f
Ala97
Thr98
Ile99
Ile100
Val101
Met102
Val77
Ser76
Phe78
Thr79
Ile82
Trp81
Asn83
Asp84
Met86
Ser85

684

685

686 **Supplementary Figure 4: Map qualities of different CIS^{Sc} modules.**

687 **a-f.** Local resolution maps of the CIS^{Sc} baseplate with C6 symmetry (a), CIS^{Sc} baseplate with
688 C3 symmetry (c), and the CIS^{Sc} cap with C6 symmetry (e). (d-f) shows regions of the cryoEM
689 density map (mesh) that were superimposed with the atomic models (ribbons and sticks),
690 demonstrating the agreement between the observed and modeled amino acid side chains for
691 one beta-sheet (left) and one alpha helix (right). Shown are examples of the baseplate with C6
692 symmetry (b), the baseplate with C3 symmetry (d), and the cap with C6 symmetry (f).

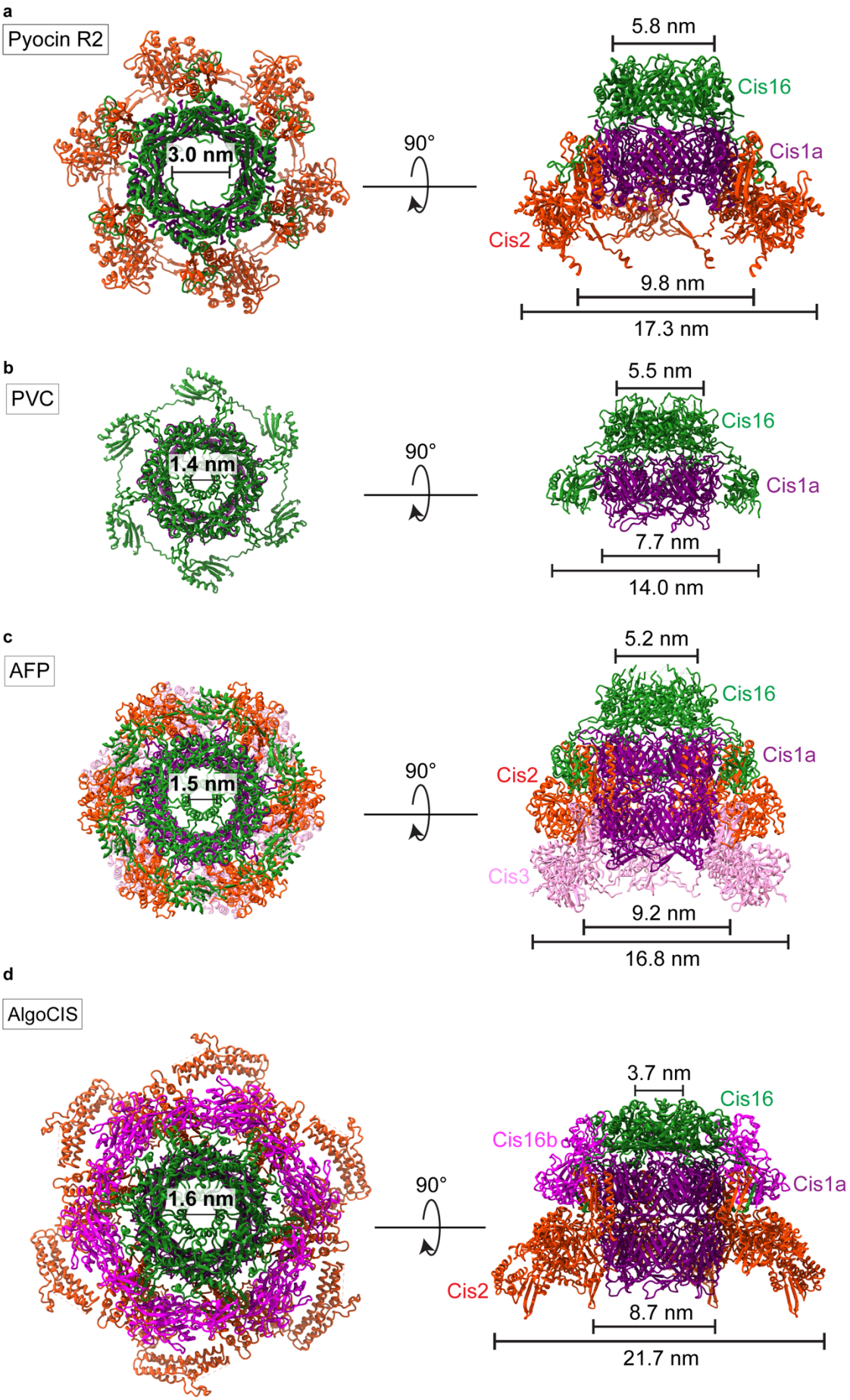
a
Pyocin R2
3.0 nm
90°
5.8 nm
Cis16
Cis1a
Cis2
9.8 nm
17.3 nm
b
PVC
1.4 nm
90°
5.5 nm
Cis16
Cis1a
7.7 nm
14.0 nm
c
AFP
1.5 nm
90°
5.2 nm
Cis16
Cis1a
Cis2
Cis3
9.2 nm
16.8 nm
d
AlgoCIS
1.6 nm
90°
3.7 nm
Cis16
Cis16b
Cis1a
Cis2
8.7 nm
21.7 nm

693

694 **Supplementary Figure 5: Structures of the cap modules of other CISs**.

695 **a-d.** Top views (left) and side views (right) of ribbon representations of the structures of CIS
696 cap modules of Pyocin R2 (a, PDB 6U5B), PVC (b, PDB 6J0N), AFP (**c**, PDB 6RAP) and
697 AlgoCIS (d, PDB 7ADZ).

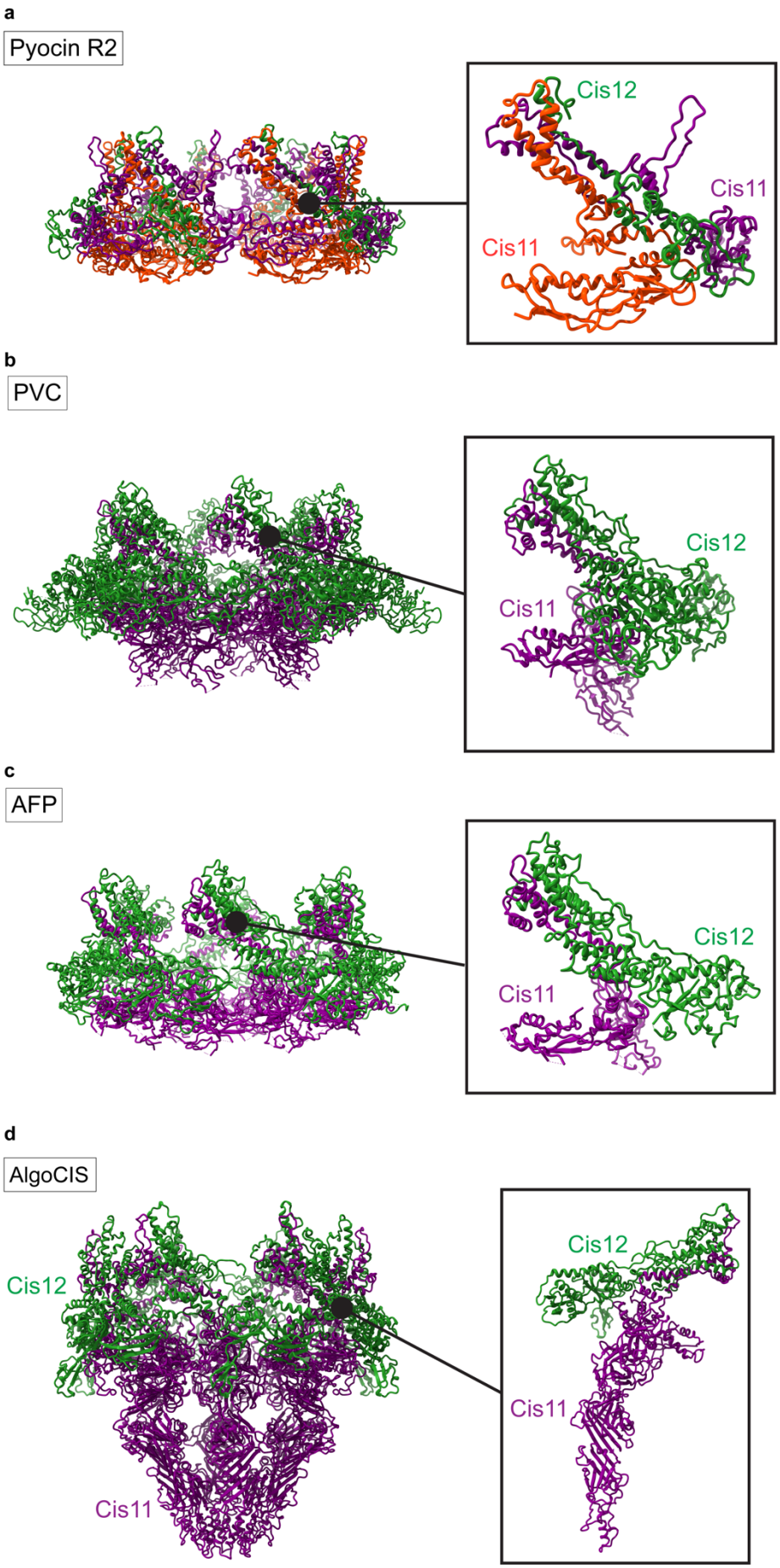
a
Pyocin R2
Cis12
Cis11
Cis11
b
PVC
Cis12
Cis11
c
AFP
Cis12
Cis11
d
AlgoCIS
Cis12
Cis11
Cis12
Cis11

698

699 **Supplementary Figure 6: Structures of the baseplate modules of other CISs**.

700 **a-d.** Ribbon representations of the full structures (left) and the individual wedge subunit (right)
701 of the CIS baseplate components (Cis11/12) of Pyocin R2 (a, PDB 6U5F), PVC (b, PDB 6J0F),
702 AFP (c, PDB 6RAO) and AlgoCIS (d, PDB 7AEB).

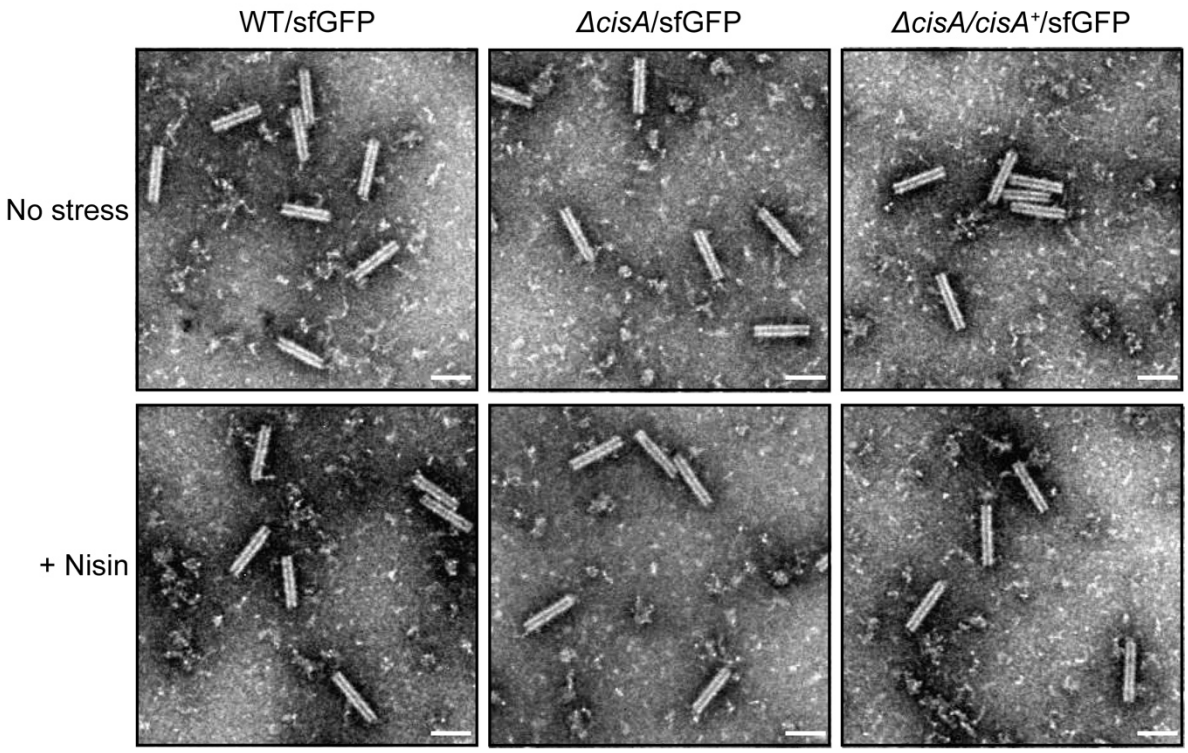

703

704 **Supplementary Figure 7: Control experiment showing that CIS^{Sc} particles are**
705 **comparable in the strains used in the viability assay.**

706 Representative negative-stain electron micrographs of purified CIS^{Sc} particles from the
707 WT/sfGFP, the Δ*cisA*/sfGFP mutant and the Δ*cisA*/Δ*cisA*$^{+}$/sfGFP complemented mutant
708 exposed to no stress (upper row) or 1 µg/ml nisin (lower row). No differences were observed
709 between the overall structure of CIS^{Sc} particles. These experiments were performed three
710 independent times. Bars, 100 nm.

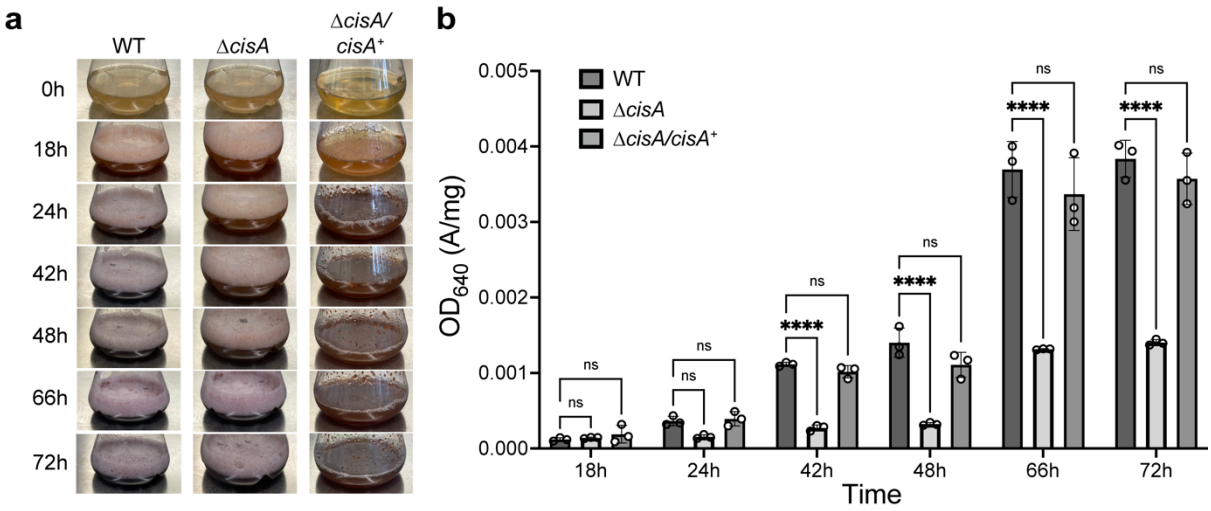

Supplementary Figure 8: CisA impacts secondary metabolite production.

a. Comparison of cultures of WT, Δ*cisA* mutant and Δ*c*isA/Δ*cisA*$^{+}$ mutant in R2YE liquid medium. The coloration of the culture is indicative of actinorhodin (purple) and undecylprodigiosin (red) production (33). Images of each culture flask were taken at the indicated time points.

b. Quantification of total actinorhodin production by the strains shown in (a), revealing reduced production in the Δ*cisA* mutant. Samples were taken at the indicated time points. Actinorhodin was extracted and quantified by measuring the optical density OD_{640} of the culture supernatant (65) and normalized to the wet pellet weight. Analysis was performed in biological triplicate experiments. The mean values and standard error are shown. ns (not significant) and **** ($p < 0.0001$) were calculated using one-way ANOVA and Tukey's post-test.

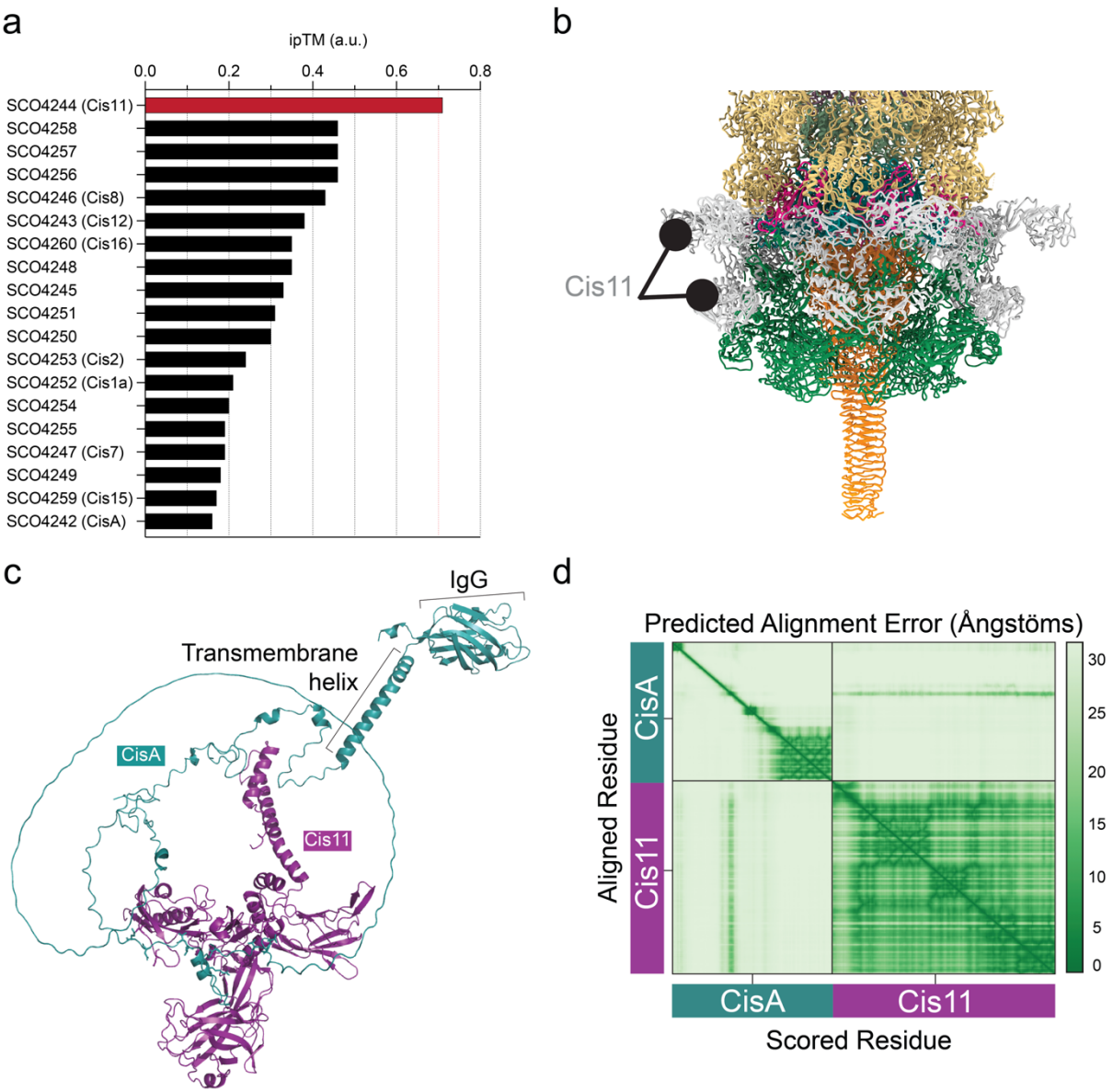

723

724 **Supplementary Figure 9: *In silico* protein-protein interaction analyses predict that CisA**
725 **binds a CIS^{Sc} baseplate component.**

726 **a.** An AlphaFold2-Multimer-based protein-protein interaction screen between monomeric
727 CisA and the 19 gene products of the CIS^{Sc} gene cluster suggests an interaction between CisA
728 and the baseplate component Cis11. The likelihood of a protein-protein interaction was ranked
729 based on the interface pTM (ipTM) confidence score, with an ipTM greater than 0.7 indicating
730 a potential protein-protein interaction.

731 **b.** Zoomed-in view of the SPA-cryoEM structure of the CIS^{Sc} baseplate complex (Fig. 2b/d),
732 illustrating the peripheral and surface-exposed position of Cis11.

733 **c/d** Predicted CisA-Cis11 complex. (c) The Alphafold3 model of the CisA-Cis11 complex. The
734 "IgG" domain at the C-terminal end of CisA is located in the periplasm. (d) The Alphafold3
735 predicted aligned error (%) heatmap plot of the concatenated Cis11 and CisA input sequence.

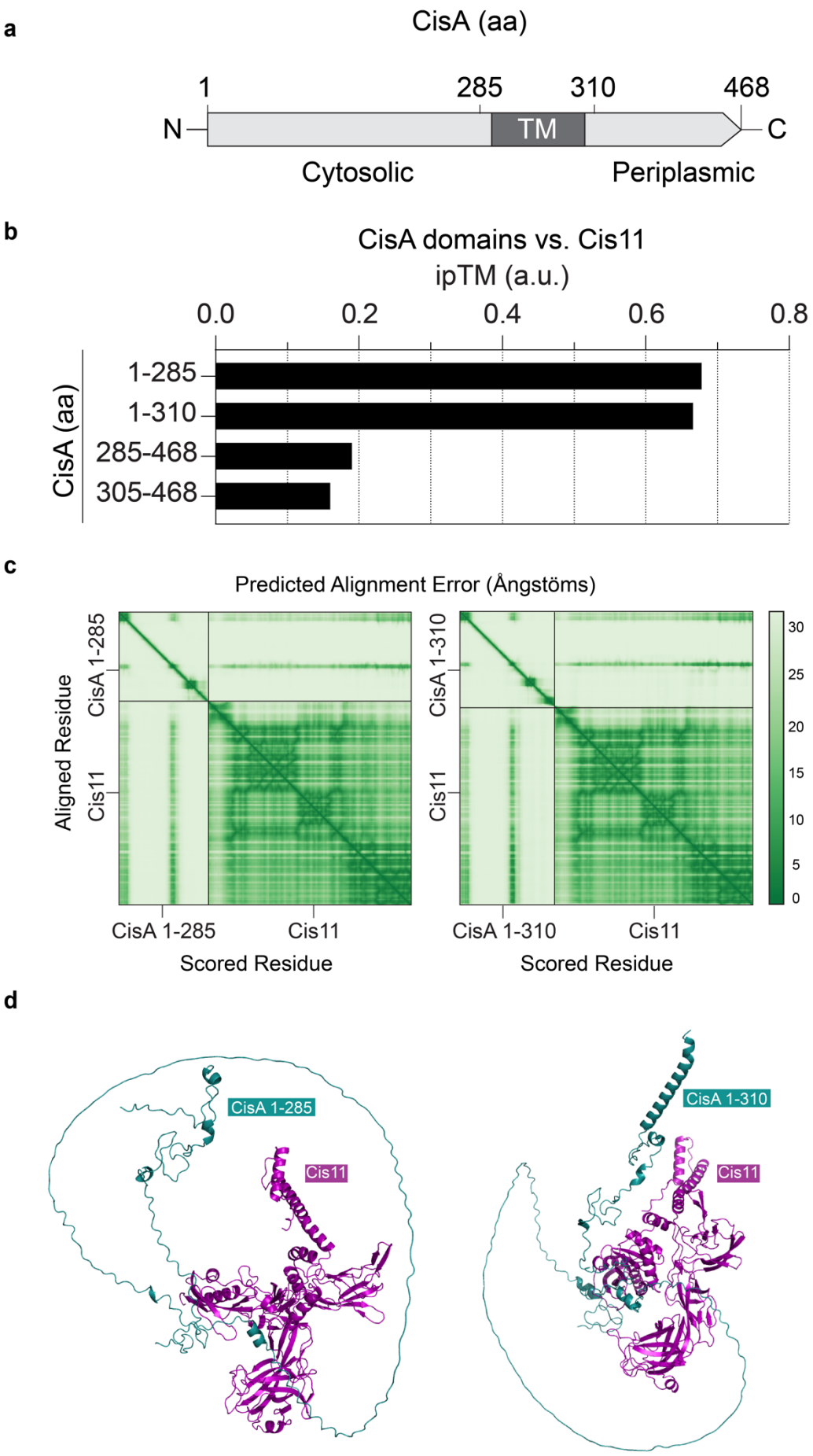
a
CisA (aa)
1
285
310
468
N
TM
C
Cytosolic
Periplasmic
b
CisA domains vs. Cis11
ipTM (a.u.)
0.0
0.2
0.4
0.6
0.8
CisA (aa)
1-285
1-310
285-468
305-468
c
Predicted Alignment Error (Ångstöms)
Aligned Residue
CisA 1-285
Cis11
CisA 1-285
Cis11
Scored Residue
CisA 1-310
Cis11
CisA 1-310
Cis11
Scored Residue
30
25
20
15
10
5
0
d
CisA 1-285
Cis11
CisA 1-310
Cis11

736

737 **Supplementary Figure 10: The cytosolic part of CisA is predicted to interact with Cis11.**

738 **a.** Schematic showing the CisA domain organization. Relevant amino acid (aa) positions
739 are shown above. TM, transmembrane domain.
740 **b.** AlphaFold2-Multimer based protein-protein interaction screen between monomers of
741 CisA and truncated versions of CisA and Cis11. The likelihood of a protein-protein
742 interaction was ranked based on the interface pTM (ipTM) confidence score.
743 **c/d.** Predicted CisA-Cis11 complexes using truncated versions of CisA (amino acids 1-285 and
744 1-310) show that the largely unstructured cytosolic portion of CisA is required to interact with
745 Cis11. (c) The Alphafold3 predicted aligned error (%) heatmap plot of the concatenated Cis11
746 and truncated CisA 1-285 and CisA 1-310 input sequences. (d) The Alphafold3 model of the
747 CisA 1-285-Cis11 (left) and CisA 1-310-Cis11 (right) complexes.

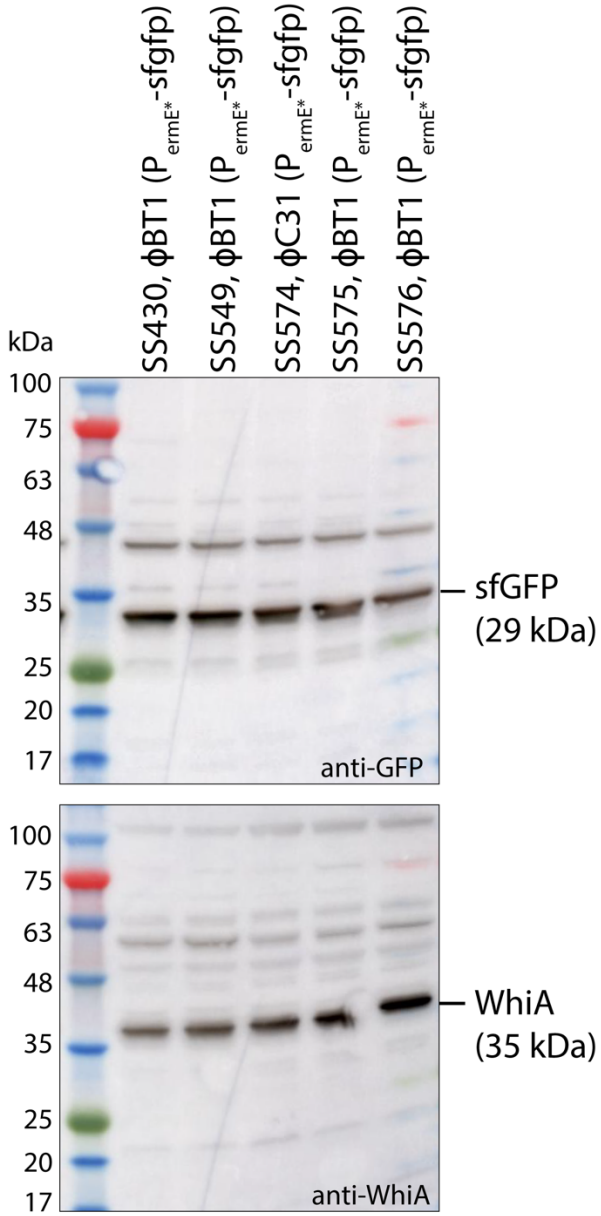

Supplementary Figure 11: Western blot confirming similar levels of cytosolic sfGFP in strains used for viability assays.

Control experiments to verify similar protein levels of sfGFP which was expressed either from the ϕC31 or the ϕBT1 phage attachment site in the *S. coelicolor* genome. Expression of *sfgfp* was driven from the constitutive *ermE** promoter (P_{ermE*}). Equal amounts of total protein were loaded and sfGFP levels were detected with an anti-GFP antibody. As a control, the same cell lysates were also probed with an anti-WhiA antibody. Shown are representative results of duplicate experiments.

757 # References

758 1. Lin L. The expanding universe of contractile injection systems in bacteria. Curr Opin
759 Microbiol. 2024 Jun 1;79:102465.

760 2. Brackmann M, Nazarov S, Wang J, Basler M. Using Force to Punch Holes: Mechanics of
761 Contractile Nanomachines. Trends Cell Biol. 2017 Sep;27(9):623–32.

762 3. Taylor NMI, van Raaij MJ, Leiman PG. Contractile injection systems of bacteriophages and
763 related systems. Mol Microbiol. 2018 Apr;108(1):6–15.

764 4. Taylor NMI, Prokhorov NS, Guerrero-Ferreira RC, Shneider MM, Browning C, Goldie KN,
765 et al. Structure of the T4 baseplate and its function in triggering sheath contraction. Nature.
766 2016 May 19;533(7603):346–52.

767 5. Böck D, Medeiros JM, Tsao HF, Penz T, Weiss GL, Aistleitner K, et al. In situ architecture,
768 function, and evolution of a contractile injection system. Science. 2017 Aug
769 18;357(6352):713–7.

770 6. Allsopp LP, Bernal P. Killing in the name of: T6SS structure and effector diversity.
771 Microbiology. 2023;169(7):001367.

772 7. Coulthurst S. The Type VI secretion system: a versatile bacterial weapon. Microbiol Read
773 Engl. 2019 May;165(5):503–15.

774 8. Chen L, Song N, Liu B, Zhang N, Alikhan NF, Zhou Z, et al. Genome-wide Identification
775 and Characterization of a Superfamily of Bacterial Extracellular Contractile Injection
776 Systems. Cell Rep. 2019 Oct 8;29(2):511-521.e2.

9. Geller AM, Pollin I, Zlotkin D, Danov A, Nachmias N, Andreopoulos WB, et al. The extracellular contractile injection system is enriched in environmental microbes and associates with numerous toxins. Nat Commun. 2021 Jun 18;12(1):3743.

10. Basler M, Pilhofer M, Henderson GP, Jensen GJ, Mekalanos JJ. Type VI secretion requires a dynamic contractile phage tail-like structure. Nature. 2012 Feb 26;483(7388):182–6.

11. Durand E, Nguyen VS, Zoued A, Logger L, Péhau-Arnaudet G, Aschtgen MS, et al. Biogenesis and structure of a type VI secretion membrane core complex. Nature. 2015 Jul;523(7562):555–60.

12. Zachs T, Malit JJL, Xu J, Schürch A, Sivabalasarma S, Nußbaum P, et al. Archaeal type six secretion system mediates contact-dependent antagonism [Internet]. bioRxiv; 2024 [cited 2024 Jun 19]. p. 2024.04.11.588991. Available from: https://www.biorxiv.org/content/10.1101/2024.04.11.588991v1

13. Xu J, Ericson CF, Lien YW, Rutaganira FUN, Eisenstein F, Feldmüller M, et al. Identification and structure of an extracellular contractile injection system from the marine bacterium Algoriphagus machipongonensis. Nat Microbiol. 2022 Mar;7(3):397–410.

14. Shikuma NJ, Pilhofer M, Weiss GL, Hadfield MG, Jensen GJ, Newman DK. Marine tubeworm metamorphosis induced by arrays of bacterial phage tail-like structures. Science. 2014 Jan 31;343(6170):529–33.

15. Hurst MRH, Beard SS, Jackson TA, Jones SM. Isolation and characterization of the Serratia entomophila antifeeding prophage. FEMS Microbiol Lett. 2007 May;270(1):42–8.

798 16. Jiang F, Li N, Wang X, Cheng J, Huang Y, Yang Y, et al. Cryo-EM Structure and Assembly
799 of an Extracellular Contractile Injection System. Cell. 2019 Apr 4;177(2):370-383.e15.

800 17. Weiss GL, Eisenstein F, Kieninger AK, Xu J, Minas HA, Gerber M, et al. Structure of a
801 thylakoid-anchored contractile injection system in multicellular cyanobacteria. Nat
802 Microbiol. 2022 Mar;7(3):386–96.

803 18. Casu B, Sallmen JW, Schlimpert S, Pilhofer M. Cytoplasmic contractile injection systems
804 mediate cell death in Streptomyces. Nat Microbiol. 2023 Apr;8(4):711–26.

805 19. Vladimirov M, Zhang RX, Mak S, Nodwell JR, Davidson AR. A contractile injection
806 system is required for developmentally regulated cell death in Streptomyces coelicolor.
807 Nat Commun. 2023 Mar 16;14(1):1469.

808 20. Nagakubo T, Yamamoto T, Asamizu S, Toyofuku M, Nomura N, Onaka H. Phage tail-like
809 nanostructures affect microbial interactions between Streptomyces and fungi. Sci Rep.
810 2021 Oct 11;11:20116.

811 21. Nagakubo T, Asamizu S, Yamamoto T, Kato M, Nishiyama T, Toyofuku M, et al.
812 Intracellular Phage Tail-Like Nanostructures Affect Susceptibility of Streptomyces
813 lividans to Osmotic Stress. mSphere. 2023 Apr 11;8(3):e00114-23.

814 22. Nagakubo T, Nishiyama T, Yamamoto T, Nomura N, Toyofuku M. Contractile injection
815 systems facilitate sporogenic differentiation of Streptomyces davawensis through the
816 action of a phage tapemeasure protein-related effector. Nat Commun. 2024 May
817 24;15(1):4442.

818 23. Schlimpert S, Elliot MA. The Best of Both Worlds—Streptomyces coelicolor and
819 Streptomyces venezuelae as Model Species for Studying Antibiotic Production and
820 Bacterial Multicellular Development. J Bacteriol. 2023 Jun 22;205(7):e00153-23.

821 24. Flärdh K, Buttner MJ. Streptomyces morphogenetics: dissecting differentiation in a
822 filamentous bacterium. Nat Rev Microbiol. 2009 Jan;7(1):36–49.

823 25. Desfosses A, Venugopal H, Joshi T, Felix J, Jessop M, Jeong H, et al. Atomic structures
824 of an entire contractile injection system in both the extended and contracted states. Nat
825 Microbiol. 2019 Nov 1;4(11):1885–94.

826 26. Rybakova D, Schramm P, Mitra AK, Hurst MRH. Afp14 is involved in regulating the
827 length of Anti-feeding prophage (Afp). Mol Microbiol. 2015;96(4):815–26.

828 27. Ge P, Scholl D, Prokhorov NS, Avaylon J, Shneider MM, Browning C, et al. Action of a
829 minimal contractile bactericidal nanomachine. Nature. 2020 Apr;580(7805):658–62.

830 28. Jumper J, Evans R, Pritzel A, Green T, Figurnov M, Ronneberger O, et al. Highly accurate
831 protein structure prediction with AlphaFold. Nature. 2021 Aug;596(7873):583–9.

832 29. Alexeyev MF, Winkler HH. Membrane topology of the Rickettsia prowazekii ATP/ADP
833 translocase revealed by novel dual pho-lac reporters 1 1Edited by G. von Heijne. J Mol
834 Biol. 1999 Jan;285(4):1503–13.

835 30. Ramos-León F, Bush MJ, Sallmen JW, Chandra G, Richardson J, Findlay KC, et al. A
836 conserved cell division protein directly regulates FtsZ dynamics in filamentous and
837 unicellular actinobacteria. Kana BD, Garner EC, editors. eLife. 2021 Mar 17;10:e63387.

838 31. Bibb MJ, Domonkos A, Chandra G, Buttner MJ. Expression of the chaplin and rodlin
839 hydrophobic sheath proteins in Streptomyces venezuelae is controlled by σ(BldN) and a
840 cognate anti-sigma factor, RsbN. Mol Microbiol. 2012 Jun;84(6):1033–49.

841 32. Malpartida F, Hopwood DA. Molecular cloning of the whole biosynthetic pathway of a
842 Streptomyces antibiotic and its expression in a heterologous host. Nature. 1984
843 May;309(5967):462–4.

844 33. Tsao SW, Rudd BA, He XG, Chang CJ, Floss HG. Identification of a red pigment from
845 Streptomyces coelicolor A3(2) as a mixture of prodigiosin derivatives. J Antibiot (Tokyo).
846 1985 Jan;38(1):128–31.

847 34. Rapisarda C, Cherrak Y, Kooger R, Schmidt V, Pellarin R, Logger L, et al. In situ and
848 high-resolution cryo-EM structure of a bacterial type VI secretion system membrane
849 complex. EMBO J. 2019 May 15;38(10):e100886.

850 35. Lien YW, Amendola D, Lee KS, Bartlau N, Xu J, Furusawa G, et al. Mechanism of
851 bacterial predation via ixotrophy [Internet]. bioRxiv; 2024 [cited 2024 Jun 19]. p.
852 2024.01.29.577165. Available from:
853 https://www.biorxiv.org/content/10.1101/2024.01.29.577165v1

854 36. Bongiovanni TR, Latario CJ, Le Cras Y, Trus E, Robitaille S, Swartz K, et al. Assembly
855 of a unique membrane complex in type VI secretion systems of Bacteroidota. Nat
856 Commun. 2024 Jan 10;15(1):429.

857 37. Ouyang R, Ongenae V, Muok A, Claessen D, Briegel A. Phage fibers and spikes: a
858 nanoscale Swiss army knife for host infection. Curr Opin Microbiol. 2024 Feb
859 1;77:102429.

860 38. Weiss GL, Eisenstein F, Kieninger AK, Xu J, Minas HA, Gerber M, et al. Structure of a
861 thylakoid-anchored contractile injection system in multicellular cyanobacteria. Nat
862 Microbiol. 2022 Mar;7(3):386–96.

863 39. McLean TC. LazyAF, a pipeline for accessible medium-scale *in silico* prediction of
864 protein-protein interactions [Internet]. 2024 [cited 2024 Jun 19]. Available from:
865 http://biorxiv.org/lookup/doi/10.1101/2024.01.29.577767

866 40. T. Kieser M. J. Bibb M. J. Buttner K. F. Chater and D. A. Hopwood. Practical Streptomyces
867 Genetics. Norwich: John Innes Foundation; 2000.

868 41. Gust B, Challis GL, Fowler K, Kieser T, Chater KF. PCR-targeted Streptomyces gene
869 replacement identifies a protein domain needed for biosynthesis of the sesquiterpene soil
870 odor geosmin. Proc Natl Acad Sci U S A. 2003 Feb 18;100(4):1541–6.

871 42. Gust B, Chandra G, Jakimowicz D, Yuqing T, Bruton CJ, Chater KF. Lambda red-
872 mediated genetic manipulation of antibiotic-producing Streptomyces. Adv Appl
873 Microbiol. 2004;54:107–28.

874 43. Ohi M, Li Y, Cheng Y, Walz T. Negative Staining and Image Classification - Powerful
875 Tools in Modern Electron Microscopy. Biol Proced Online. 2004;6:23–34.

876 44. Bush MJ, Bibb MJ, Chandra G, Findlay KC, Buttner MJ. Genes Required for Aerial
877 Growth, Cell Division, and Chromosome Segregation Are Targets of WhiA before
878 Sporulation in Streptomyces venezuelae. mBio. 2013 Sep 24;4(5):e00684-13.

879 45. Gallego JJ, Severi E, Chandra G, Palmer T. Identification of novel tail--anchored
880 membrane proteins integrated by the bacterial twin--arginine translocase.

881 46. Zheng SQ, Palovcak E, Armache JP, Verba KA, Cheng Y, Agard DA. MotionCor2:
882 anisotropic correction of beam-induced motion for improved cryo-electron microscopy.
883 Nat Methods. 2017 Apr;14(4):331–2.

884 47. Afanasyev P, Ravelli RBG, Matadeen R, De Carlo S, van Duinen G, Alewijnse B, et al. A
885 posteriori correction of camera characteristics from large image data sets. Sci Rep. 2015
886 Jun 11;5(1):10317.

887 48. P. Afanasyev. CryoEM tools [Internet]. 2023. Available from:
888 https://github.com/afanasyevp/cryoem_tools

889 49. Punjani A, Rubinstein JL, Fleet DJ, Brubaker MA. cryoSPARC: algorithms for rapid
890 unsupervised cryo-EM structure determination. Nat Methods. 2017 Mar 1;14(3):290–6.

891 50. Wagner T, Merino F, Stabrin M, Moriya T, Antoni C, Apelbaum A, et al. SPHIRE-
892 crYOLO is a fast and accurate fully automated particle picker for cryo-EM. Commun Biol.
893 2019 Jun 19;2(1):1–13.

894 51. Scheres SHW. RELION: implementation of a Bayesian approach to cryo-EM structure
895 determination. J Struct Biol. 2012 Dec;180(3):519–30.

896 52. Weiss GL, Medeiros JM, Pilhofer M. In Situ Imaging of Bacterial Secretion Systems by
897 Electron Cryotomography. Methods Mol Biol Clifton NJ. 2017;1615:353–75.

898 53. Mastronarde DN. Automated electron microscope tomography using robust prediction of
899 specimen movements. J Struct Biol. 2005 Oct;152(1):36–51.

900 54. Kremer JR, Mastronarde DN, McIntosh JR. Computer visualization of three-dimensional
901 image data using IMOD. J Struct Biol. 1996 Feb;116(1):71–6.

902 55. Tegunov D, Cramer P. Real-time cryo-electron microscopy data preprocessing with Warp.
903 Nat Methods. 2019 Nov;16(11):1146–52.

904 56. Emsley P, Lohkamp B, Scott WG, Cowtan K. Features and development of Coot. Acta
905 Crystallogr D Biol Crystallogr. 2010 Apr;66(Pt 4):486–501.

906 57. Song Y, DiMaio F, Wang RYR, Kim D, Miles C, Brunette T, et al. High-resolution
907 comparative modeling with RosettaCM. Struct Lond Engl 1993. 2013 Oct 8;21(10):1735–
908 42.

909 58. Adams PD, Afonine PV, Bunkóczi G, Chen VB, Davis IW, Echols N, et al. PHENIX: a
910 comprehensive Python-based system for macromolecular structure solution. Acta
911 Crystallogr D Biol Crystallogr. 2010 Feb;66(Pt 2):213–21.

912 59. Schindelin J, Arganda-Carreras I, Frise E, Kaynig V, Longair M, Pietzsch T, et al. Fiji - an
913 Open Source platform for biological image analysis. Nat Methods. 2012 Jun
914 28;9(7):10.1038/nmeth.2019.

915 60. Ef P, Td G, Cc H, Gs C, Dm G, Ec M, et al. UCSF Chimera--a visualization system for
916 exploratory research and analysis. J Comput Chem [Internet]. 2004 Oct [cited 2022 May
917 17];25(13). Available from: https://pubmed.ncbi.nlm.nih.gov/15264254/

918 61. Goddard TD, Huang CC, Meng EC, Pettersen EF, Couch GS, Morris JH, et al. UCSF
919 ChimeraX: Meeting modern challenges in visualization and analysis. Protein Sci Publ
920 Protein Soc. 2018 Jan;27(1):14–25.

921 62. Mirdita M, Schütze K, Moriwaki Y, Heo L, Ovchinnikov S, Steinegger M. ColabFold:
922 making protein folding accessible to all. Nat Methods. 2022 Jun;19(6):679–82.

923 63. O'Reilly FJ, Graziadei A, Forbrig C, Bremenkamp R, Charles K, Lenz S, et al. Protein
924 complexes in cells by AI -assisted structural proteomics. Mol Syst Biol. 2023 Apr
925 12;19(4):e11544.

926 64. Madeira F, Madhusoodanan N, Lee J, Eusebi A, Niewielska A, Tivey ARN, et al. The
927 EMBL-EBI Job Dispatcher sequence analysis tools framework in 2024. Nucleic Acids Res.
928 2024 Jul 5;52(W1):W521–5.

929 65. Zhang Y, Wang L, Zhang S, Yang H, Tan H. hmgA, transcriptionally activated by HpdA,
930 influences the biosynthesis of actinorhodin in Streptomyces coelicolor. FEMS Microbiol
931 Lett. 2008 Mar;280(2):219–25.

932

933